REALTIDE

This project has received funding from the European Union's Horizon 2020 research and innovation programme under Grant Agreement No 727689

Document Title:
D3.5 - Report on Synthetic Load Spectra and Time Series Development

Document No:
RLT-WP3-5-PDL-001-02

Status Code	Description
A	Accepted
B	Issued for Acceptance
C	Issued for Review
D	Information Only Approval not required
E	Cancelled

02	B	Issued for Acceptance	Miguel Angel Valdivia Camacho	Jeffrey Steynor	Stephane Paboeuf & Antonio Fernández Díez
01	C	1st Draft for Review	Miguel Angel Valdivia Camacho	Jeffrey Steynor	NA
01	D	Original version	Miguel Angel Valdivia Camacho	Jeffrey Steynor	NA
Rev No	Status	Revision Description	Prepared By / Date	Reviewed By / Date	Approved By / Date

European Commission
H2020 Programme for Research & Innovation

Advanced monitoring, simulation, and control of tidal devices in unsteady, highly turbulent realistic tide environments

Grant Agreement number: 727689

Project Acronym: RealTide

Project Title: Advanced monitoring, simulation, and control of tidal devices in unsteady, highly turbulent realistic tide environments

Deliverable 3.5 (D3.5)
Synthetic Load Spectra and Time Series of Tidal Turbines
WP3
Realistic Simulation of Tidal Turbine

WP Leader: The University of Edinburgh (UEDIN)

Dissemination level: Public

Summary: This report describes Deliverable 3.5 and details the work of Task 3.5 within WP3 of RealTide. As the main objective of the task requires a non-dimensional load spectra and time series dataset to assist future developers in tidal stream turbine design decisions, datasets available from different test setups have been collected and categorised. Based on the information available from these tests, 21 non-dimensional coefficients are proposed to make these test measurements independent from their turbine designs and flow conditions. The proposed non-dimensional variables take information both from the input measurements as well as internal forces calculated in this analysis based on static equilibrium linear equations, thus common test data, such as thrust and torque, are used to make this easily applicable for future tests. The load spectra and time series have been developed in relation to the tip speed ratio (TSR) of 10 tank tests. These normalised base datasets have successfully been correlated when compared to different datasets from both numerical models and commercial tests. All the non-dimensional coefficients and ratios are presented in both the time domain and the frequency domain for developers to not only consider static load cases but also dynamic loads that impact the fatigue life of the different key components of tidal turbines. The density distribution curves as well as the frequency spectra of these coefficients can be recreated with the produced datasets of this task, which have been stored in the Edinburgh DataShare portal.

Objectives: Present the Deliverable 3.5. Describe the datasets available, surrounding the turbine properties, control parameters and flow conditions. Describe the equations developed under static equilibrium to find all the internal forces in the structure. Describe the non-dimensional variables proposed to normalise the datasets. Describe the spectra generation methods and the normalised dataset format. Present the normalised non-dimensional variables in both the time domain and the frequency domain. Present the correlation between datasets from different test conditions. Prepare a report to present the process and discuss the conclusions.

Table of Contents

List of Figures

List of Tables

1. INTRODUCTION

The objective of the WP3 "Realistic Simulation of Tidal Turbines", led by The University of Edinburgh (UEDIN), is to numerically simulate the ocean environment, the tidal energy converter (TEC), and the electrical system under realistic working conditions. The model construct is driven by a turbulent inflow boundary condition and has been calibrated in order to provide a reliable simulation tool. The results from the simulations are validated against experimental measurements from WP2 "Realistic Tidal Environment". In WP3, three approaches have been considered:

- T3.1 Tide-to-wire model.
- T3.2 Blade resolved CFD model.
- T3.3 BEMT-CFD model.

These approaches have been considered in order to determine which of the models have the lowest computational cost in regard of the targeted objective and the highest representation of the realistic conditions. An ideal simulator should be able to generate accurate results with a low computational cost.

As a result of the realistic simulations, time series of load spectrums can be generated which in turn will be used to understand the causes of failure of the TEC components with the aim to design fault-tolerant devices. The dataset of synthetic loads will be used in WP4 "Advanced monitoring strategies" and WP5 "Novel and advanced components".

For instance, the data generated by the BEMT-CFD model, time series for load spectra, will be used in this report (T3.5 – development of synthetic load spectra), WP4, and WP5. A representation of the data paths can be seen in Figure 1, turning the data from a time domain to a frequency domain for all the TEC components.

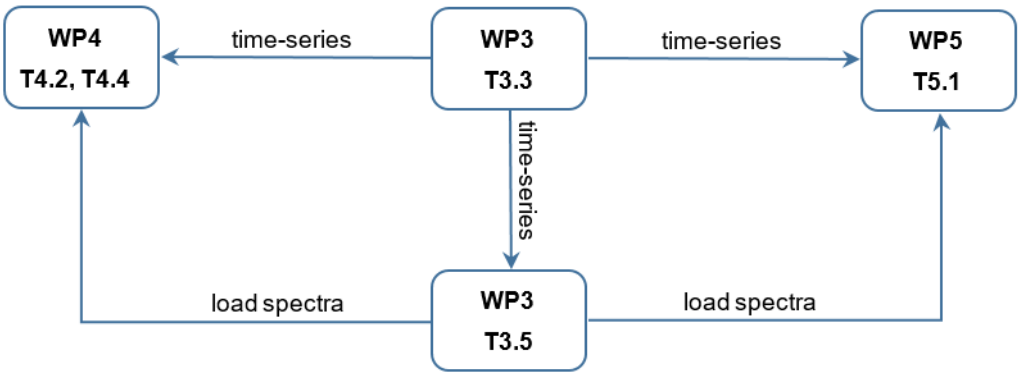

Figure 1 - Task alignment with relevant work packages [1].

This report explains the steps taken to complete the deliverable D3.5 and it starts with a description of the two input datasets that will be processed throughout this task. The first batch of datasets are experimental test results run in the FloWave facility, where specific instrumentation has been used to capture the loads acting on the turbine structure. Additionally, the process of calibration and validation of the results is explained. The second dataset is part of the deliverable D3.3 and it is obtained from the CFD/BEMT model used. Both datasets consider the same generic TEC as a specimen, therefore, a comparison is achievable, and correlation can be quantified. As for the geometry properties of this specimen, a CAD model has been regenerated to take global positions accurately in all coordinates. The use of a CAD model achieves a clear representation of the whole structure to analyse all the component forces and moments through a selection of free body diagrams (FBD). Once all the input data has been processed for analysis, other external forces acting on the structure are isolated by the differences between loads at different measurement locations. The technique developed with the generic TEC has been applied to some of the load and power coefficients of the Sabella D10 and D12 turbine shown in Figure 2.

Figure 2 – Tidal turbine tested at FloWave (left) and Sabella D10 before deployment (right) [2].

After all the internal forces and key derived variables have been calculated, non-dimensional coefficients are calculated to normalise the turbine load and performance parameters. These ratios and coefficients will show high recurrent values across all devices and act as a guide for future designs, where minimum information such as the tip speed ratio (TSR) will generate practical estimations. The time series of these key variables are then converted to the rotational frequency domain to generate spectra that is comparable between different devices and operational speed.
Lastly, all devices are analysed and correlated to find links between the variability of the non-dimensional ratios and other much more common coefficients, such as power coefficients, thrust coefficients, torque coefficients, and TSR. The coefficients can be rescaled to any TEC to predict fatigue or static loading in steady state conditions. Conclusions around key components of tidal turbines are drawn based on the results and findings about the dependence on other variables are discussed.

1.1 Abbreviations & Definitions

BEMT	Blade Element Momentum Theory
BV	Bureau Veritas
BV M&O	Bureau Veritas Marine & Offshore
CAD	Computer Aided Design
CFD	Computational Fluid Dynamics
EO	EnerOcean
FBD	Free Body Diagram
FFT	Fast Fourier Transform
GA	Grant Agreement
HATT	Horizontal Axis Tidal Turbine
HO	HydrOcean
IFR	Ifremer (Institut Français pour la Recherche et l'Exploitation de la Mer)
ISSA	Ingeteam Power Technology
PMP	Project Management Plan
RBM	Root Bending Moment
RPM	Revolutions per Minute
SAB	Sabella
1-T	1-Tech
TEC	Tidal Energy Converter
TSR	Tip Speed Ratio
UEDIN	The University of Edinburgh
WP	Work Package

1.2 References

[1] A. Ortega, J. Shek, D. Ingram, S. Loubeyre, and E. Nicolas, "D3.5 - Report on Synthetic Load Spectra and Time Series Development," 2019.
[2] Sabella, "Sabella D10 - France," 2019. https://www.sabella.bzh/en/projects/d10 (accessed Jan. 12, 2021).
[3] G. S. Payne, T. Stallard, and R. Martinez, "Design and manufacture of a bed supported tidal turbine model for blade and shaft load measurement in turbulent flow and waves," *Renew. Energy*, vol. 107, pp. 312–326, Jul. 2017, doi: 10.1016/j.renene.2017.01.068.
[4] The University of Edinburgh, "Edinburgh DataShare." https://datashare.ed.ac.uk/ (accessed Mar. 17, 2021).
[5] A. Ortega, J. P. Tomy, J. Shek, S. Paboeuf, and D. Ingram, "An Inter-Comparison of Dynamic, Fully Coupled, Electro-Mechanical, Models of Tidal Turbines," *Energies*, vol. 13, no. 20, p. 5389, Oct. 2020, doi: 10.3390/en13205389.
[6] J. Marcille, "MONITOR Ifremer test tanks," Quimper, 2019.
[7] J. Marcille, "Personal Communication." 2021.
[8] J. V. Nunes De Sousa, R. Lins De Macêdo, W. Ferreira De Amorim Junior, and A. Gilson Barbosa De Lima, "Numerical Analysis of Turbulent Fluid Flow and Drag Coefficient for Optimizing the AUV Hull Design," *Open J. Fluid Dyn.*, vol. 4, pp. 263–277, 2014, doi: 10.4236/ojfd.2014.43020.
[9] T. Thiringer and J. Å. Dahlberg, "Periodic pulsations from a three-bladed wind turbine," *IEEE Trans. Energy Convers.*, vol. 16, no. 2, pp. 128–133, Jun. 2001, doi: 10.1109/60.921463.
[10] S. Das, N. Karnik, and S. Santoso, "Time-Domain Modeling of Tower Shadow and Wind Shear in Wind Turbines," *ISRN Renew. Energy*, vol. 2011, pp. 1–11, Oct. 2011, doi: 10.5402/2011/890582.
[11] UCAR Community Programs, "Unidata | NetCDF." https://www.unidata.ucar.edu/software/netcdf/ (accessed Jan. 20, 2021).

1.3 Distribution List

This Document is a RealTide Internal Document and is classified as an Internal Report. It is for distribution solely within the RealTide Consortium.

It can be distributed if all Beneficiaries, represented by the General Assembly, give approval.

2. DESIGN SPECIFICATIONS

This chapter contains four categories: the turbine specifications, the experimental FloWave data, the CFD-BEMT data, and lastly, the dataset acquired from two Sabella turbines, D10 and D12. The CFD-BEMT code and tests run in FloWave use the same turbine design geometry.

2.1 Turbine Model Design

The generic tidal turbine has been used in numerous tests over the years and has the geometry properties shown in Table 1.

Table 1 – Turbine specifications for the generic tidal turbine at FloWave [3].

Description	Variable	Value
Number of blades	n_{blades}	3.000
Rotor diameter (m)	D_{rot}	1.200
Nacelle's front diameter (m)	D_{nac1}	0.120
Nacelle's back diameter (m)	D_{nac2}	0.160
Hub height (m)	h_{hub}	1.012
Nose cone to tower distance (m)	l_{hub}	0.590
Rotor plane to tower distance (m)	l_{rot}	0.486
Position of moment relative to the top surface of the loading cell (m)	lc_{centre}	0.042971
Distance between nacelle and tower joint (m)	Δ_n	0.02105

Any other relevant geometry property can be seen in the CAD files attached in the Edinburgh DataShare portal [4]. The CAD model has been simplified; thus, it does not consider bolt holes nor internal components.

2.2 Experimental FloWave Data

The experimental data acquired belongs to a tidal turbine structure that has been used in many tests at the FloWave facility, with a typical test or inflow velocity of 0.8 m s^{-1} [3]. This generic turbine has been equipped with torque and thrust instrumentation that provides high quality measurements upstream of any bearings or seals, hence any noise, perturbation or parasitic effects are minimised.

There are three different kinds of transducers in the structure. The first one is the root-bending moment transducer that acts as a joint between the blades and the hub, as seen in Figure 3. Measurements are taken within the middle of the square section of the transducer, 13.3 mm from the root of the blade, this has not been transposed to the actual root of the blade.

Another transducer is located on the main shaft, and measures the torque and thrust of the rotor.

Lastly, the whole structure is fixed to a load cell GEN 5 made by AMTI, which acts as a multi-axis force transducer that can measure the individual reactions in 6 degrees of freedom. There are 10 datasets available that will be studied and normalised, which are shown in Table 3, along with their tip speed ratio (TSR). These tests consider a flow stream with a set turbulence intensity, however, do not consider waves or off axis flows in their loading profile.

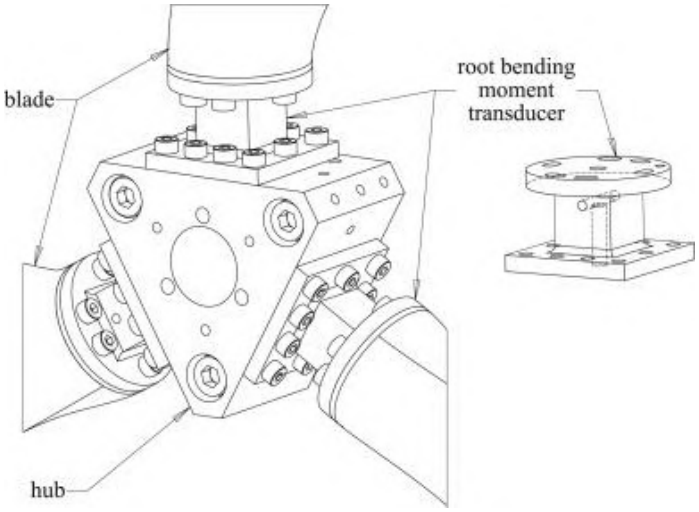

Figure 3 – Root-bending moment transducer location [3].

Once a test is run with all the transducers installed on the specimen, the variables that are stored for processing are shown in Table 2. Although there are more variables measured throughout the test, only the key ones to D3.5 have been gathered from the overall results. After all this data is processed, variables might change notations to indicate the difference of the variables' source.

Table 2 – Measured variables in tank tests.

Location	Variable	Notation
General	Time	$Time$
	Angular speed	RPM
	Polar position	θ
Blade	Flapwise root bending moment	$RBM0, RBM1, RBM2$
Rotor	Torque	TRQ
	Thrust	THR
Foundation	Surge, sway, heave	$LCFX, LCFY, LCFZ$
	Roll, pitch, yaw	$LCMX, LCMY, LCMZ$

The key forces and moments measured follow a global coordinate system, except for the root bending moment transducers. These moments are considered as flapwise root bending moments which only account for the thrust exerted on each blade, meaning that they are the resultant moments in the z and y coordinates of the rotor plane. Figure 4 provides a visualization of the whole interaction of these forces and moments and their respective locations. Sign and direction of these forces are designated based on the flow direction, which for this dataset follows the positive x-direction.

Table 3 – Experimental tank tests run in the FloWave Facility.

Internal Test ID	TSR
TA0012	3.0
TA0009	4.5
TA0013	5.0
TA0015	6.6
TA0001	7.1
TA0011	7.6
TA0016	8.1
TA0008	9.1
TA0010	10.1
TA0014	12.1

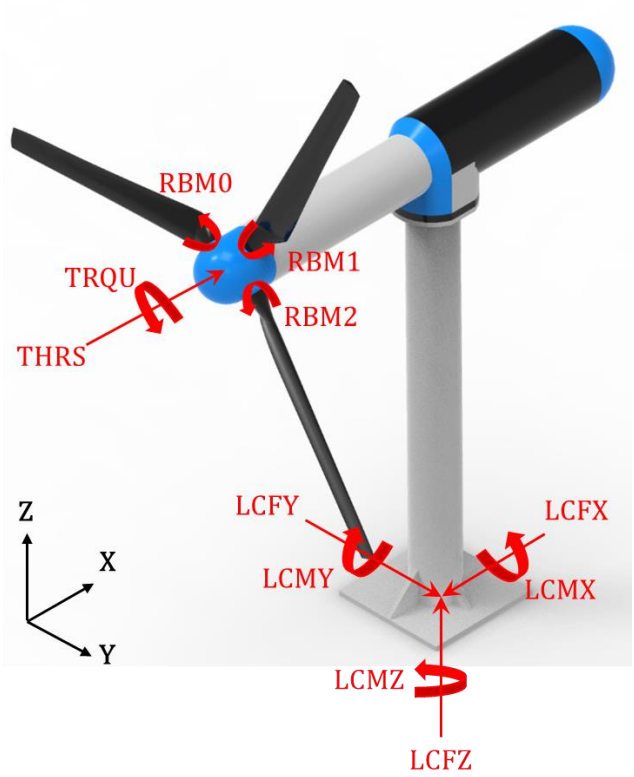

Figure 4 – Location of forces and reactions measured in FloWave tank tests.

Analysing the root bending moments (RBMs), as they are the only measurements not locked to a single global coordinate, an offset has been noted between the average of the RBM on each blade, as seen in Figure 5. In this figure, where the data has been filtered to 10 Hz for visualisation purposes only, the average of the RBM measurement on blade 2 is offset. This discrepancy is possibly due to small errors in the pitch angle when the blades are installed on the rotor. Undesired residual moments in other directions along the structure are the result of these anomalies, which in turn might decrease the fatigue life of the whole turbine.

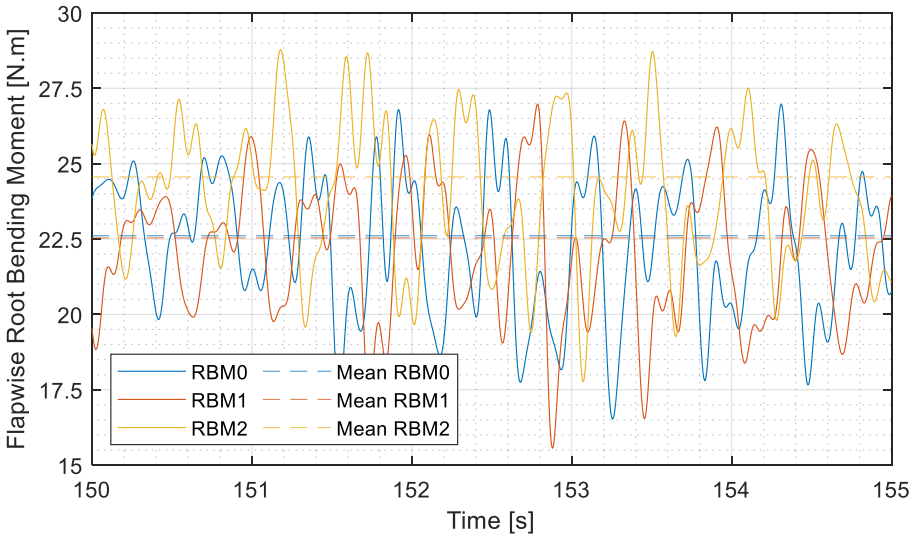

Figure 5 – Root bending moments for the experimental data at 0.8 m s^{-1}.

Therefore, the difference in RBMs is mean corrected for further processing and analysis to get an accurate normalisation. This correction consists of shifting the average of every blade to a common value, so the mean of every blade has the same amplitude. The result of a mean correction and a 10Hz filter for visualisation purposes only can be seen in Figure 6, where the average of the three RBMs have been set to the same amplitude, eliminating the systematic error produced at the assembly phase. This correction can also reduce inaccuracies regarding centres of effort of the axial forces.

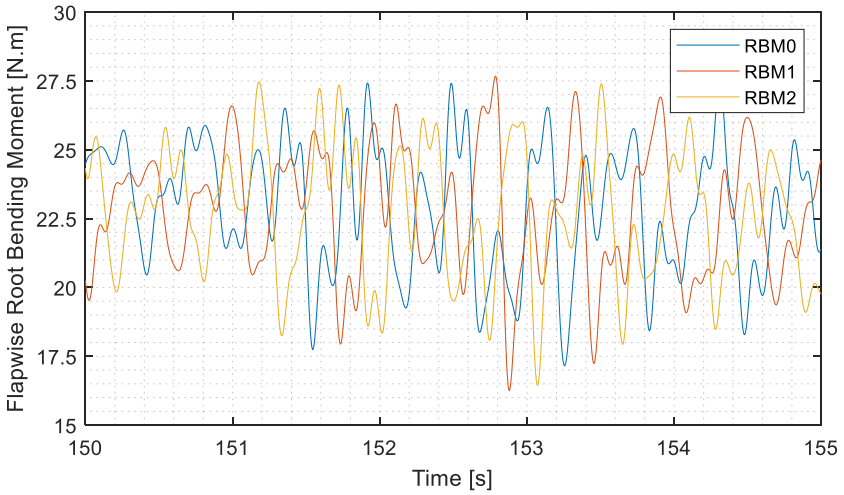

Figure 6 – Root bending moments on the test tanks after correction.

2.3 CFD-BEMT Data

In task 3.3 (T3.3), a model of a TEC coupled with a model of an electrical system has been built. Computational Fluid Dynamics (CFD) was used to simulate realistic behaviour of the ocean environment, and Blade Element Momentum Theory (BEMT) has been used to represent the hydrodynamics of the turbine blades. The turbine model is fed by realistic upstream turbulent inflow, calibrated, and validated using data from WP2 (T2.2), which generates a turbulent intensity equivalent to 10% [5]. Data has been generated from this code using 5 different upstream flow velocities, from 0.6 to 1.0 m s^{-1}, which can be seen in Figure 7 and Figure 8. Data from both figures have been filtered for frequencies lower than 25 Hz for visualisation purposes only.

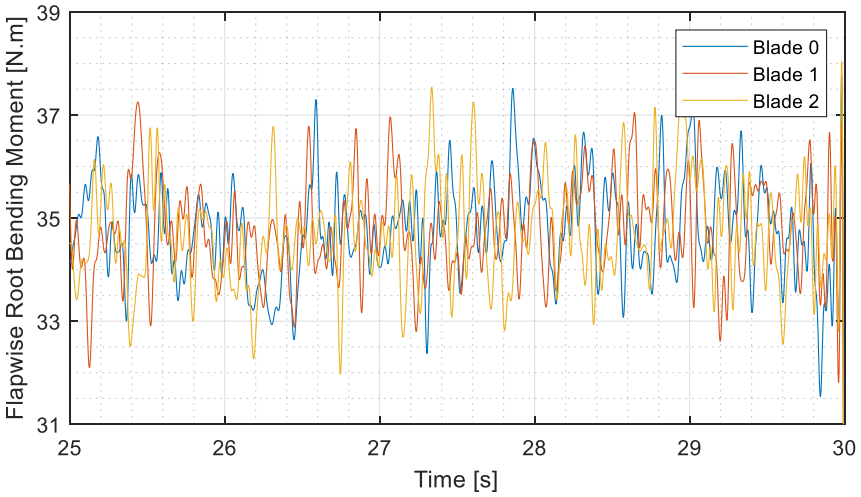

Figure 7 – Root bending moments for a 0.8 m s^{-1} upstream flow velocity.

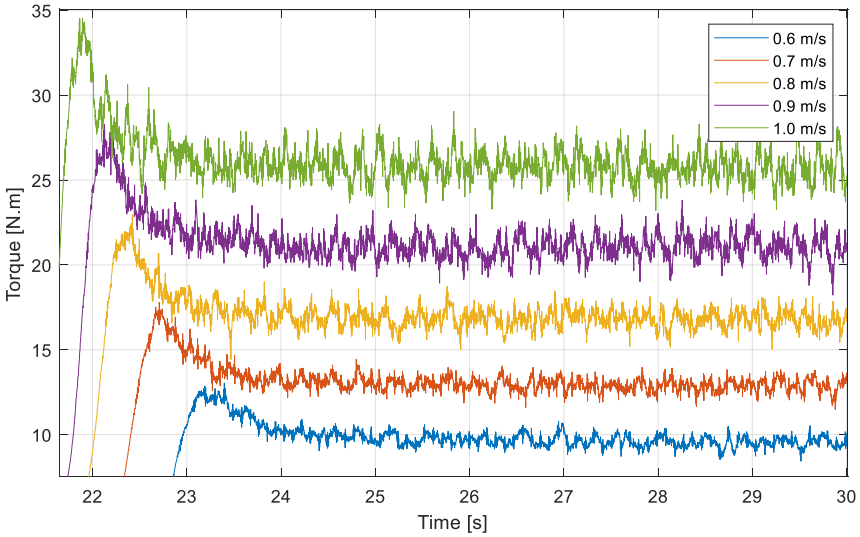

Figure 8 – Torque at different upstream flow velocities.

Since this data has been generated from a model in which only the blades are interacting with the flow, other sources of drag forces have been neglected, such as the ones generated from the nacelle and the tower structures. The key variables obtained from this dataset are shown in Table 4 with their respective notation in the input files. As mentioned before, the tidal turbine geometry properties are similar between this dataset and the dataset available from the FloWave tank tests.

Table 4 – Output variables from the CFD-BEMT code in T3.3.

Variable	Notation
General	
Time	$Time$
Angular speed	RPM
Polar position	θ
Power generation	P
Thrust force	THR
Total torque	TRQ
Blade	
Flapwise root bending moment	$RBM0, RBM1, RBM2$
Drag forces	F_{drag}
Lift forces	F_{lift}
Axial forces	F_{ax}
Tangential forces	F_{tan}

For this scenario, the thrust is not the sum of all the forces acting in the rotor along the flow direction, hence it does not consider the drag force of the nacelle. The location of the thrust and torque is considered to be at the centre of the rotor swept area, as the rest are located all on the blades, as shown in Figure 9. The existence of the forces acting directly on the blades makes this model more reliable if they want to be translated to the foundation, however, in key coordinates, the magnitude of the reaction forces will not reach the actual forces under real conditions. A further analysis will show the true impact of drag forces acting on the other structure components aside from the blades, especially in the moment generated by the surge at the foundation.

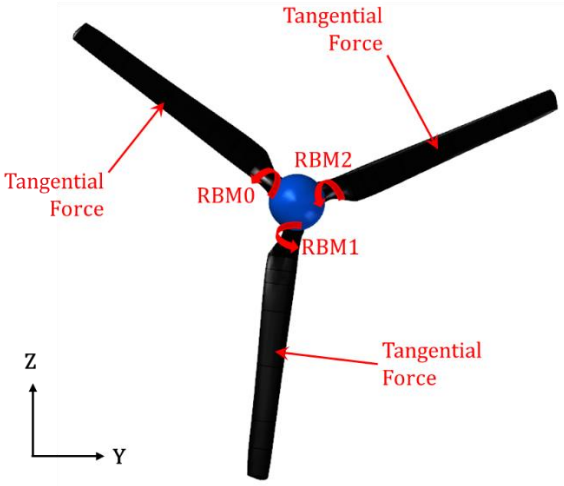

Figure 9 – Location of forces and moments measured in the CFD-BEMT code.

2.4 Sabella D10 and D12 Data

Defined TSR and bulk velocity datasets have been acquired from Sabella to find correlation between different turbine designs along several of the proposed non-dimensional coefficients on the next chapter. These Sabella datasets belong to two turbine designs, D10 and D12, each one of them with different geometry properties and flow conditions, which can be seen in Table 5.

Table 5 – Sabella D10 and D12 turbine and flow specifications [3,4].

Description	Variable	D10	D12
Number of blades	n_{blades}	6	5
Bulk velocity (m/s)	U	2.0	1.4
Tip Speed Ratio	TSR	2.5	-
Rotor diameter (m)	D_{rot}	0.4	0.6
Nacelle's front diameter (m)	D_{nac1}	-	0.18
Hub height (m)	h_{hub}	-	1.0
Nose cone to tower distance (m)	l_{hub}	-	-
Rotor plane to tower distance (m)	l_{rot}	-	0.21

Both tests were run on scaled models, D10 having a 1/25th scale and the D12 turbine scaled to 1/20th. As seen in Figure 10, the tower structure is different from the generic tidal turbine at FloWave. The D10 test had the current tower design, whereas the D12 test was fixed from the top, considering solely the nacelle and rotor to be similar to the full design.

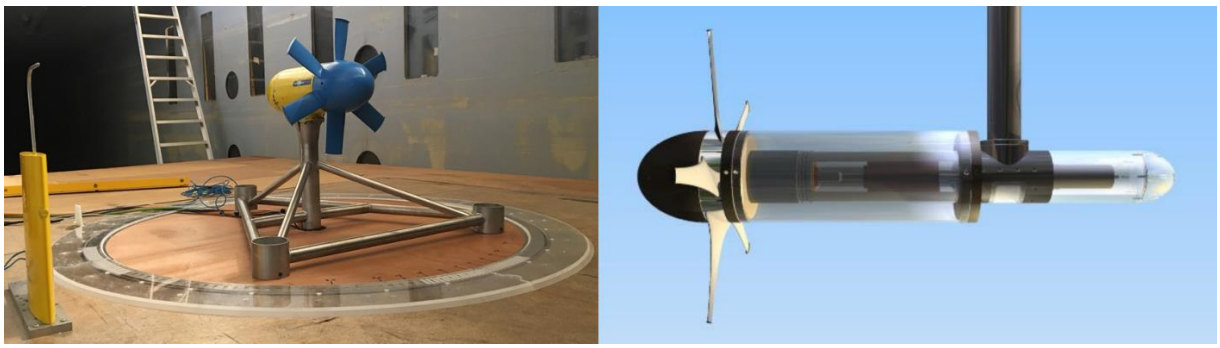

Figure 10 – Sabella D10 and D12 scaled tank tests [5,6].

In the same manner, the forces and moments measured varies for both tests, as shown in Table 6. Additionally, a turbulence intensity rate of 15% has been included in the test specifications for the D12

tank test. As for the D10 tank test the TSR was set to 2.5, which is the maximum value that can be reached for this specific rotor. During the test, a leakage forced the addition of pressure inside the nacelle, where the thrust sensor is located, leading to unreliable readings at the rotor [7].

Table 6 – Variables measured at Sabella D10 and D12 tank tests [6].

Description	Abbreviation	D10	D12
Rotor rotational speed	RPM	Measured	Measured
Thrust	THR	Measured	Measured
Torque	TRQ	Measured	Measured
Reaction force at blade root	$R_b \begin{bmatrix} x \\ y \end{bmatrix}$	-	Measured
Reaction moment at blade root	$M_b \begin{bmatrix} x \\ y \\ z \end{bmatrix}$	-	Measured
Reaction force at foundation	$\begin{bmatrix} LCFX \\ LCFY \end{bmatrix}$	Measured	-

The reaction moment and forces on the D12 tank test does not represent the measurements of each individual blade. This is due to the transducer equipment available being suitable only for a 3-bladed rotor. Therefore, blade supports had to be manufactured to adapt the transducer clamp to the D12 design. As seen in Figure 11, the blade support achieves an accurate measurement of one of the blades, whereas the measurement of the other two transducers would result in a cumulative, and therefore not representative, sum of forces and moments in 2 blades at the same time.

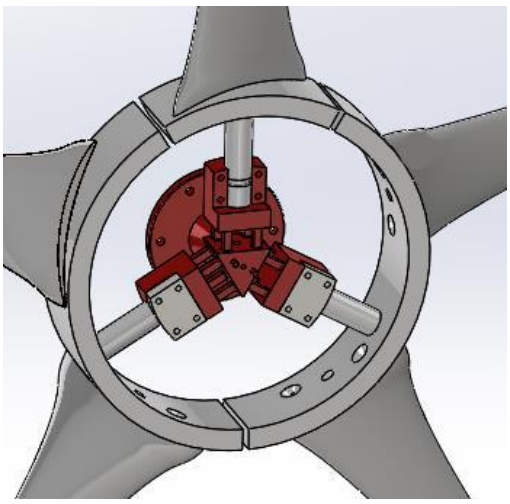

Figure 11 – Blade supports for the Sabella D12 tank test [6].

3. DESIGN PRINCIPLES

3.1 Derived Variables

Although the different turbines in this report do not share the same design, the rotors follow the same principles. The geometric variables used standard naming conventions to enable easy comparison between different sources of data. Rotor area, blade length, instantaneous power, TSR, and centre of effort can be calculated with the following equations:

Rotor Area (m)
$$A = \frac{\pi D_{rot}^2}{4} \quad (1)$$

Blade Length (m)
$$R = \frac{D_{rot} - D_{nac1}}{2} \quad (2)$$

Instantaneous Power (W)
$$P = T\omega = TRQ \frac{RPM\ 2\pi}{60[s]} \quad (3)$$

Tip Speed Ratio (-)
$$TSR = \frac{\omega R}{U} \quad (4)$$

Flapwise Centre of Effort (m)
$$CE_i = \frac{RBMi}{THR/n_{blades}} \quad (5)$$

Where D_{rot} is the rotor diameter, D_{nac1} is the nacelle front diameter, ω is the angular speed, TRQ is the rotor torque, RPM is the rotational speed, U is the upstream flow velocity, $RBMi$ is the defined flapwise RBM of a blade, and THR is the rotor thrust. The thrust is divided by the number of blades. In the upcoming sections, other derived variables are calculated based on the information available from the different datasets.

3.1.1 FloWave Tank Tests

Through subtraction of measured forces is it possible to calculate the drag forces exerted on the structure between the rotor and the foundation, in this case a drag force located in the nacelle and another one located in the tower. The tower drag force is based in the difference between the thrust that is measured at the nacelle and the reaction force in the x-direction measured at the load cell. This is only valid when the yaw angle is zero. Both forces can be compared in Figure 12 and negative values, which were reduced by filtering the data below 10 Hz, can be accounted as wake and vortex effects.

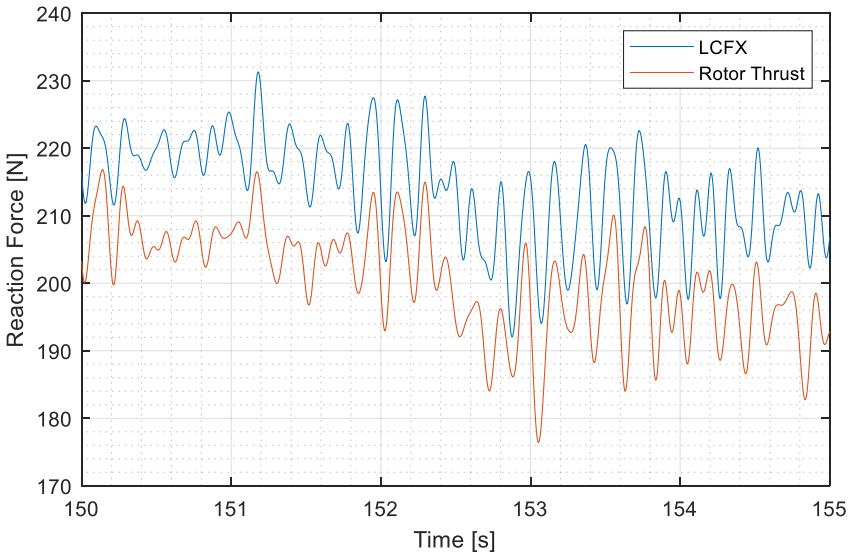

Figure 12 – Load cell reaction force in the x-direction compared to rotor thrust.

As mentioned before, the rotor thrust measured represents the sum of both the blades and the nosecone drag forces. To estimate the nosecone drag force, equation 6 can be used based on body shape effects. Naturally, an ellipsoid under these flow conditions would have a drag coefficient of approximately 0.12 [8], however, the complexity of the nacelle's shape suggests a drag coefficient of 0.5 to be adopted.

$$F_{drag} = \frac{1}{2} C_D \rho U^2 A \tag{6}$$

$$F_{drag} = \frac{1}{2}\,(0.5)\left(1000\,\frac{kg}{m^3}\right)\left(0.8\,\frac{m}{s}\right)^2 \pi \frac{(0.12\ m)^2}{4} = 1.81\ N$$

It has been noted that several datasets of previous tests taken in FloWave have missing rotation angles for the different blades. The only information available is the offset angle of the nacelle when one of the blades is at a completely vertical position when the whole structure is stalled. This offset angle will be added to the angle of each blade and an adjustment to set the horizontal axis as the reference axis of rotation to make the script more reliable regarding transitions between polar and cartesian planes. The angle between blades in the generic tidal turbine specimen is 120 degrees.

3.1.2 CFD-BEMT Numerical Model

For the numerical model to generate appropriate results in D3.3, each blade has been divided in 20 elements. In the middle of each of these elements a resultant for both the axial and tangential forces is calculated. Although this can still be solved using the static equilibrium equations, a resultant for all the elements at an equivalent centre of effort would simplify the equations used for processing the data. As the RBMs are only measured in the flapwise direction, the centre of effort for the resultant axial force can be found by dividing it by the sum of all the axial forces applied on the blade, as show in equation 7. On the other hand, the tangential force's centre of effort can be found by matching the reaction moment with the sum of all the tangential forces applied on load, following equation 10. The reaction moment can be calculated, assuming all the elements along the blade have the same length, as a sum of the individual tangential forces with their respective moment arm, resulting in equation 8.

$$CE_{ax} = \frac{RBMi}{F_{axT}} \tag{7}$$

$$M_{bxi} = \frac{length}{2} \sum_{k=0}^{n-1} (1 + 2k)\, Ftan_n \tag{8}$$

$$M_{bxi} = Ftan_T\, CE_{tan} \tag{9}$$

$$CE_{tan} = \frac{M_{bxi}}{Ftan_T} \tag{10}$$

3.2 Static Equilibrium Equations

Treating the tidal turbine as a sole one component, a free body diagram (FBD) can be drawn transmitting the external forces to the foundation, as seen in Figure 13. Since the tangential forces are applied perpendicular to the lever arm on each of the blades, they add up to generate a torque at the rotor. However, when direction of these vectors is considered, all tangential forces cancel each other out. A similar assumption can be made about the z-direction, where the only forces that could account for a net reaction would be the weight, which is assumed to be zero.

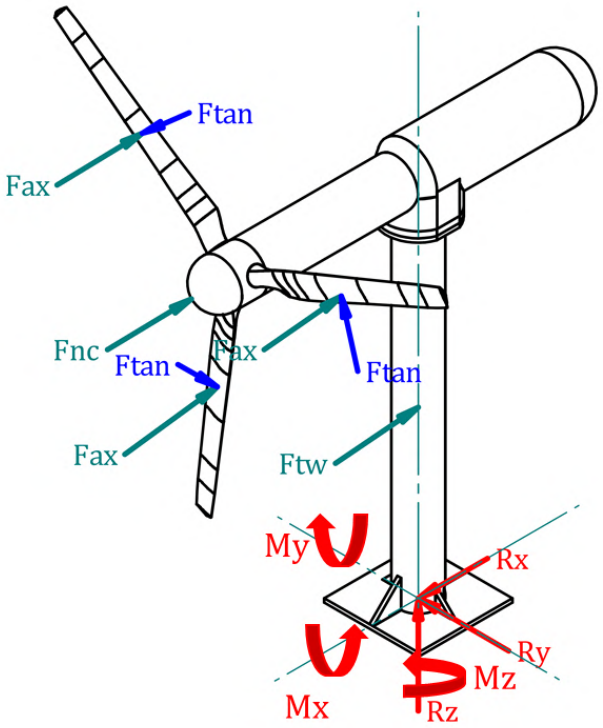

Figure 13 – FBD of a tidal turbine from an isometric view based on the CFD-BEMT data.

The equations for this simple model would show the importance of the reaction moment in the y-direction My and the reaction force in the x-direction Rx, which can be obtained from the simplification of the 3D model to a 2D one on the XZ plane, as seen in Figure 14. If the reaction forces and moments are the given data, the equations can be inverted to find the external forces experienced in the whole structure.

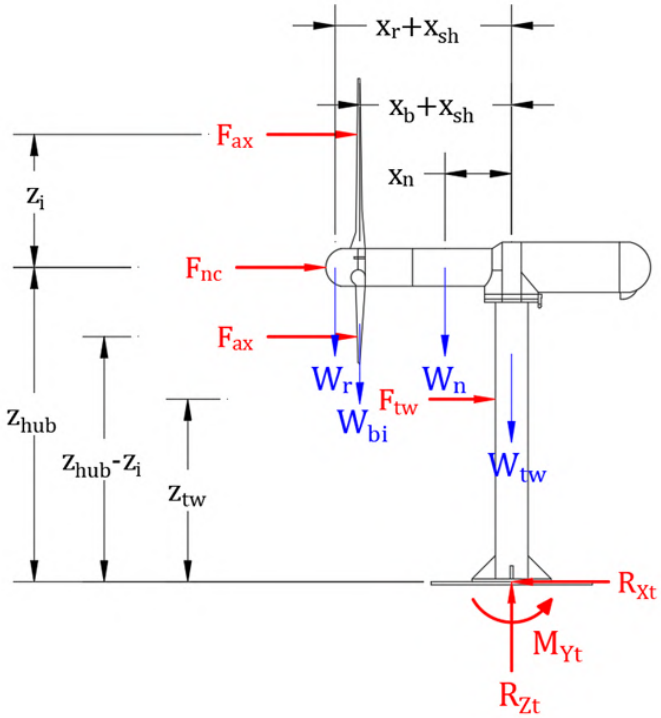

Figure 14 – External forces acting on the structure from the XZ plane.

$$\sum F_x = 0 \qquad F_{ax} + F_{ax} + F_{ax} + F_{nc} + F_{tw} - R_x = 0 \tag{11}$$

$$\sum F_z = 0 \qquad 3W_b + W_r + W_n + W_{tw} - R_z = 0 \tag{12}$$

$$\sum M_y = 0 \qquad M_y - F_{ax}(z_{hub} \pm z_i) - F_{ax}(z_{hub} \pm z_i) - F_{ax}(z_{hub} \pm z_i) + F_{nc}(z_{hub}) + F_{tw}z_{tw} + 3W_b(x_b + x_{sh}) + W_r(x_r + x_{sh}) + W_n x_n = 0 \tag{13}$$

Equations 11, 12, and 13 show a simplified analysis of static equilibrium on tidal turbines equipped with 3 blades where the axial forces are different for each blade. A comprehensive analysis regarding these forces would be dependent on the position of the blades and their corresponding angles at any given time. This variability results in residual reaction forces and moments on the other planes, which usually occurs under normal environmental conditions, however, these are not in the same order of magnitude as the surge and pitch values.

Once the tidal turbine is decomposed into several components, the effect of the external forces can be seen making their way through to the foundation. This gives the possibility to assess any component that is interacting with the whole structure and analyse the internal forces that are reacting to impede motion. For instance, four key components can be identified: the blades, the rotor, the nacelle, and the tower. All the forces interacting in these different components can be decomposed in all three directions, meaning that a matrix form of all these equations can be used to meet equilibrium appropriately. The notation for each of the components will be carried out at every instance and can be observed in Figure 16, Figure 17, Figure 18, and Figure 19. Similarly, a reference axis on each of the components needs to be located on the three global coordinates. The location of these reference axes can be observed in Figure 15, where the origin is placed at the centre of the fixed end of the tower with the load cell.

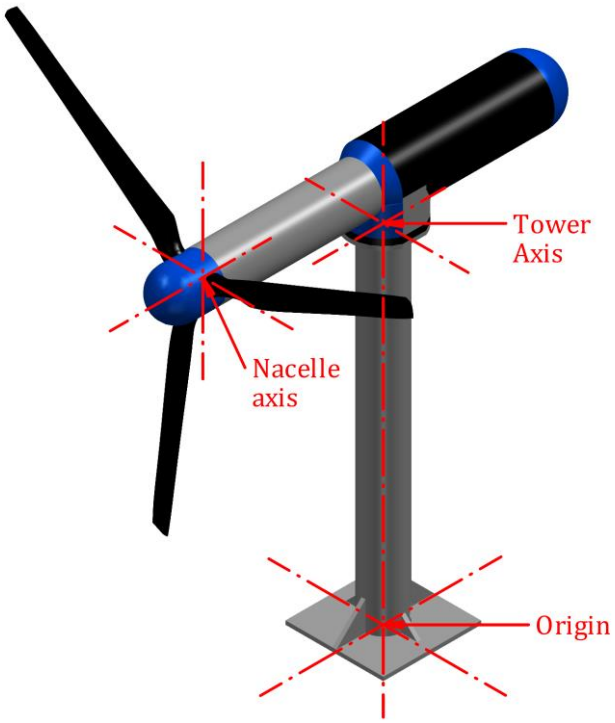

Figure 15 – Location of the different reference axes in the monopile turbine.

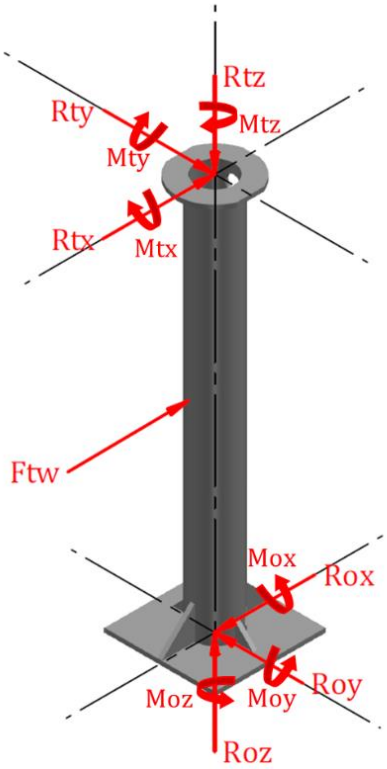

Figure 16 – Tower's free body diagram

The equations following Figure 16's FBD and considering the tower axis as the reference axis would be as shown:

$$\sum \begin{bmatrix} F_x \\ F_y \\ F_z \end{bmatrix} = 0 \qquad R_t.mag \begin{bmatrix} x \\ y \\ z \end{bmatrix} + F_{tw}.mag \begin{bmatrix} x \\ 0 \\ 0 \end{bmatrix} + R_o.mag \begin{bmatrix} x \\ y \\ z \end{bmatrix} = 0 \tag{14}$$

$$\sum \begin{bmatrix} M_x \\ M_y \\ M_z \end{bmatrix} = 0 \qquad F_{tw}.mag \begin{bmatrix} x \\ 0 \\ 0 \end{bmatrix} \left(orig - axis_n + F_{tw}.pos \begin{bmatrix} x \\ y \\ z \end{bmatrix} \right) + R_o.mag \begin{bmatrix} x \\ y \\ z \end{bmatrix} (orig - axis_n) + M_o \begin{bmatrix} x \\ y \\ z \end{bmatrix} + M_t \begin{bmatrix} x \\ y \\ z \end{bmatrix} = 0 \tag{15}$$

Since experimental data is measured from the foundation, R_t and M_t are the variables in these equations. To progress through the next component, shown in Figure 17, R_n and M_n have the same magnitude and position as R_t and M_t, respectively, but with different signs in all directions:

$$R_n = -R_t \tag{16}$$

$$M_n = -M_t \tag{17}$$

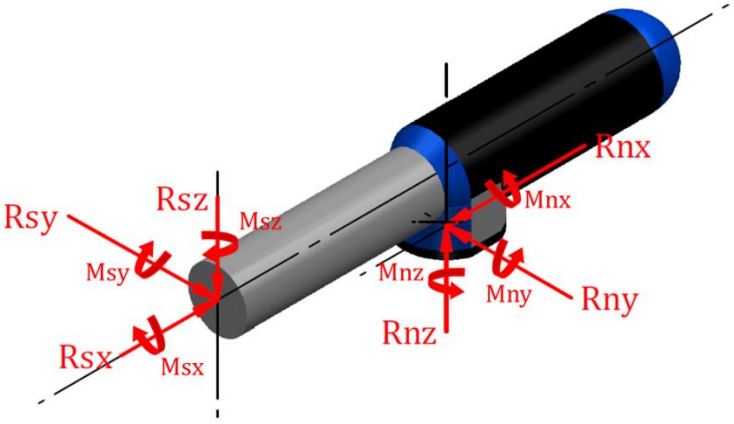

Figure 17 – Nacelle's free body diagram

Based on Figure 17, the following equations can be formulated for the forces acting on the nacelle:

$$\sum \begin{bmatrix} F_x \\ F_y \\ F_z \end{bmatrix} = 0 \qquad R_n.mag \begin{bmatrix} x \\ y \\ z \end{bmatrix} + R_s.mag \begin{bmatrix} x \\ y \\ z \end{bmatrix} = 0 \tag{18}$$

$$\sum \begin{bmatrix} M_x \\ M_y \\ M_z \end{bmatrix} = 0 \qquad R_n.mag \begin{bmatrix} x \\ y \\ z \end{bmatrix} (axis_r - axis_n) + M_s \begin{bmatrix} x \\ y \\ z \end{bmatrix} + M_n \begin{bmatrix} x \\ y \\ z \end{bmatrix} = 0 \tag{19}$$

R_s can be considered as the forces and moments that will be acting on the bearings and M_{sx} can be related to the torque measurements at the rotor. To go further on with the key components, forces and moments at the joint are equal in magnitude and opposite sign, resulting in the next formulation:

$$R_r = -R_s \tag{20}$$

$$M_r = -M_s \tag{21}$$

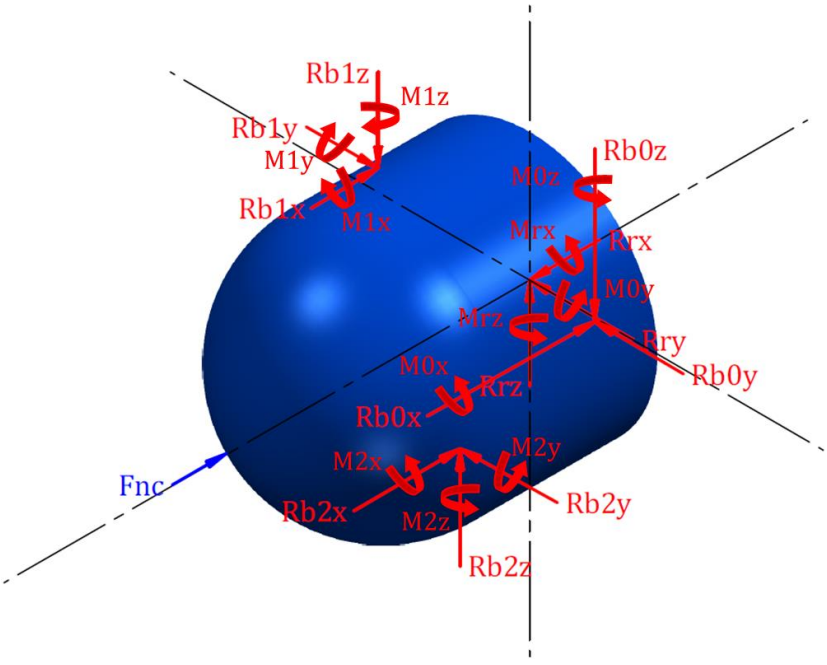

Figure 18 – Rotor's free body diagram for a 3-blade HATT

Figure 18 shows the rotor plane and has the blades attached to it through RBM transducers. This method of clamping distorts the position of the blades by a small discrepancy. For instance, the RBM measurement is located 13.3 mm inside the nacelle's diameter. The equations for this FBD are the following:

$$\sum \begin{bmatrix} F_x \\ F_y \\ F_z \end{bmatrix} = 0 \qquad R_{b0}.mag \begin{bmatrix} x \\ y \\ z \end{bmatrix} + R_{b1}.mag \begin{bmatrix} x \\ y \\ z \end{bmatrix} + R_{b2}.mag \begin{bmatrix} x \\ y \\ z \end{bmatrix} + F_{nc}.mag \begin{bmatrix} x \\ 0 \\ 0 \end{bmatrix} + R_r.mag \begin{bmatrix} x \\ y \\ z \end{bmatrix} = 0 \tag{22}$$

$$\sum \begin{bmatrix} M_x \\ M_y \\ M_z \end{bmatrix} = 0 \qquad R_{b1}.mag \begin{bmatrix} x \\ y \\ z \end{bmatrix} \left(R_{b1}.pos \begin{bmatrix} x \\ y \\ z \end{bmatrix} - R_{b0}.pos \begin{bmatrix} x \\ y \\ z \end{bmatrix} \right) + R_{b2}.mag \begin{bmatrix} x \\ y \\ z \end{bmatrix} \left(R_{b2}.pos \begin{bmatrix} x \\ y \\ z \end{bmatrix} - R_{b0}.pos \begin{bmatrix} x \\ y \\ z \end{bmatrix} \right) + F_{nc}.mag \begin{bmatrix} x \\ 0 \\ 0 \end{bmatrix} \left(F_{nc}.pos \begin{bmatrix} x \\ y \\ z \end{bmatrix} - R_{b0}.pos \begin{bmatrix} x \\ y \\ z \end{bmatrix} \right) + R_r.mag \begin{bmatrix} x \\ y \\ z \end{bmatrix} \left(R_r.pos \begin{bmatrix} x \\ y \\ z \end{bmatrix} - R_{b0}.pos \begin{bmatrix} x \\ y \\ z \end{bmatrix} \right) + M_r \begin{bmatrix} x \\ y \\ z \end{bmatrix} + M_{b0} \begin{bmatrix} x \\ y \\ z \end{bmatrix} + M_{b1} \begin{bmatrix} x \\ y \\ z \end{bmatrix} + M_{b2} \begin{bmatrix} x \\ y \\ z \end{bmatrix} = 0 \tag{23}$$

The number of blades may vary depending on the specimen, changing the size of equation 22. To find all variables in the moment's equation, the RBM measurements are needed, along with an estimation of the lever arm for each of the forces acting on the different blades. Sign alteration is applied to move on to the last FBD. Equation 23 is only an example for the reference axis placed in the transducer of the first blade and has more than one unknown variable; hence it must be projected for each one of the blades with a reference axis in the joint between the rotor and the rest of the nacelle to solve it.

$$R_b = -R_{bi} \tag{24}$$

$$M_b = -M_{bi} \tag{25}$$

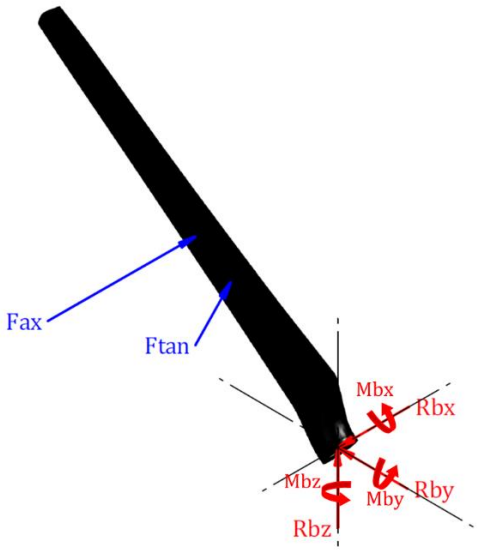

Figure 19 – Blade's free body diagram

From Figure 19, the following equations can be obtained considering both external forces applied to the blade and considering these magnitudes as a resultant of the respective distributed forces that are acting along the spanwise direction:

$$\sum \begin{bmatrix} F_x \\ F_y \\ F_z \end{bmatrix} = 0 \qquad F_{ax}.mag \begin{bmatrix} x \\ 0 \\ 0 \end{bmatrix} + F_{tan}.mag \begin{bmatrix} 0 \\ y \\ z \end{bmatrix} + R_b.mag \begin{bmatrix} x \\ y \\ z \end{bmatrix} = 0 \tag{26}$$

$$\sum \begin{bmatrix} M_x \\ M_y \\ M_z \end{bmatrix} = 0 \qquad F_{ax}.mag \begin{bmatrix} x \\ 0 \\ 0 \end{bmatrix} F_{ax}.pos \begin{bmatrix} x \\ y \\ z \end{bmatrix} + F_{tan}.mag \begin{bmatrix} 0 \\ y \\ z \end{bmatrix} F_{tan}.pos \begin{bmatrix} x \\ y \\ z \end{bmatrix} + M_b \begin{bmatrix} x \\ y \\ z \end{bmatrix} = 0 \tag{27}$$

All the equations recently developed are based on the case similar to the experimental FloWave conditions, where RBM and thrust variables are measured at the rotor and the 6 degrees of freedom are measured at the foundation. Therefore, M_{sx} and R_{sx} should be equal to the thrust and torque measured, respectively. When these equations are adapted for the CFD-BEMT model, the known variables are the axial and tangential forces which are located at each one of the blades, hence equations 26 and 27 are the starting point of the analysis until the tower equations are reached and solved.

The output of this process is organised in three different batches. The first batch contains all the information regarding the turbine measurements and the different variables that were calculated based on these values. The second batch contains all the derived non-dimensional coefficients which are discussed in the next section. Lastly, the third batch includes all the internal forces calculated in this section.

3.3 Derived Non-Dimensional Coefficients

Since all the internal and external forces calculated in Section 3.2 are specifically bounded to the specimen properties, the results are of no use to future developers unless all this information is processed into coefficients that are independent and unitless. In this sense, several coefficients and ratios have been proposed to catch key information about the load propagation along the structure, which can be seen in Table 7.

Table 7 – List of non-dimensional coefficients.

Variable	Equation	Nº
Centre of effort ratio	$CE_r = \frac{CE}{D/2}$	(28)
Tip Speed Ratio	$TSR = \frac{\omega R}{U}$	(29)
Power Coefficient	$C_P = \frac{P}{0.5\ \rho A U^3}$	(30)
Thrust Coefficient	$C_T = \frac{THR}{0.5\ \rho A U^2}$	(31)
Thrust Coefficient based on RBMs	$C_{T\_RBM} = \frac{3\ (\sum RBMi)}{0.5\ \rho \pi R^3 U^2}$	(32)
Turbine Drag Coefficient based on Surge	$C_{D\_tbs} = \frac{R_{Ox}}{0.5\ \rho A U^2}$	(33)
Turbine Drag Coefficient based on Pitch	$C_{D\_tbp} = \frac{M_{Oy}/h_{hub}}{0.5\ \rho A U^2}$	(34)

Variable	Equation	Nº
Turbine Drag Coefficient based on Sway	$C_{D\_tbsw} = \frac{R_{Oy}}{0.5\,\rho A U^2}$	(35)
Drag Coefficient on the tower	$C_{D\_tw} = \frac{R_{Ox} - THR}{0.5\,\rho(h_{tw}\,D_{tw})U^2}$	(36)
Sway to Surge Ratio	$Sw2S_r = \frac{R_{Oy}}{R_{Ox}}$	(37)
Heave to Surge Ratio	$Hv2S_r = \frac{R_{Oz} - mean(R_{Oz})}{R_{Ox}}$	(38)
Thrust to Surge Ratio	$TH2S_r = \frac{THR}{R_{Ox}}$	(39)
Surge to Pitch Ratio	$S2P_r = \frac{R_{Ox}}{M_{Oy}/h_{hub}}$	(40)
Torque to Roll Ratio	$Q2Ro_r = \frac{TRQ}{M_{Ox}}$	(41)
Torque to RBMs Ratio	$Q2BM_r = \frac{TRQ}{\sum RBMi}$	(42)
Rotor Pitch to Foundation Pitch Ratio	$RPitch_r = \frac{M_{ry}}{M_{Oy}}$	(43)
Rotor Torque to Foundation Roll Ratio	$RRoll_r = \frac{M_{rx}}{M_{Ox}}$	(44)
Rotor Yaw to Foundation Yaw Ratio	$RYaw_r = \frac{M_{rz}}{M_{Oz}}$	(45)
Rotor Centre of Effort ratio on the y-direction	$RCEy_r = \frac{M_{ry}/THR}{R}$	(46)
Rotor Centre of Effort ratio on the z-direction	$RCEz_r = \frac{M_{rz}/THR}{R}$	(47)
Tower Centre of Effort ratio on the y-direction	$TCEy_r = \frac{M_{ty}/THR}{R}$	(48)
Tower Centre of Effort ratio on the z-direction	$TCEz_r = \frac{M_{tz}/THR}{R}$	(49)

These equations will be calculated where variables are available for each dataset based on the information gathered at the input.

3.4 Spectra Generation

Once the system of equations has been solved for all datasets available for analysis, reactions and moments decomposed in the three directions are indexed and stored in MATLAB structures. Since all this information is evaluated in a time series, a fast Fourier transform (FFT) is applied to convert these loads into the frequency domain. A sample frequency is needed for an FFT to be valid, which in this case is the signal frequency of the measurement devices that have been calibrated to be equal. The frequency set for the FloWave experimental data is 256 Hz, whereas 500 Hz is the sample frequency of the CFD-BEMT dataset, and 1,000 Hz for both of Sabella tank tests [1], [3], [6]. The developed FFT

function generates sinewave properties (amplitude, spectra energy, and phi angle) of the specific variable that is being analysed. This operation is performed on all the output variables from the static equilibrium equations, as well as the non-dimensional coefficients calculated from the equations described in the previous section. Along with these output variables, information from the input data like the root bending moments of each blade, the rotor thrust, rotor torque, and instantaneous power will be converted to the frequency domain as well to gather enough information to analyse phase locking on the device. Overall, the variables that are turned into the frequency domain are:

- Root bending moments from all the blades.
- Rotor thrust and torque.
- Instantaneous power.
- Centre of effort ratios.
- Power, thrust and drag coefficients.
- Non-dimensional coefficients and ratios.
- Reaction forces and moments for blades.
- Reaction forces and moments at the shaft, from both sides.
- Reaction forces and moments at the nacelle's fixed end, from both sides.
- Reaction forces and moments at the foundation.

The upper limit at which the different variables are seen in the frequency domain is set to be at 50 Hz. This is due to heavy harmonic content in higher frequencies that can be related to mains power, which is visible in Figure 20 where the same generic turbine has been tested in an array configuration. To normalise these frequencies between different turbines, the frequency will be divided by the rotational speed. A rotational frequency domain, or P, can characterise the impact of the structure in fixed points of interest. For instance, every time a blade passes through the tower, a spike in the load amplitude can be the result and pulsations on a three-bladed turbine would be located on 3P, increasing the variation of power generated [9].

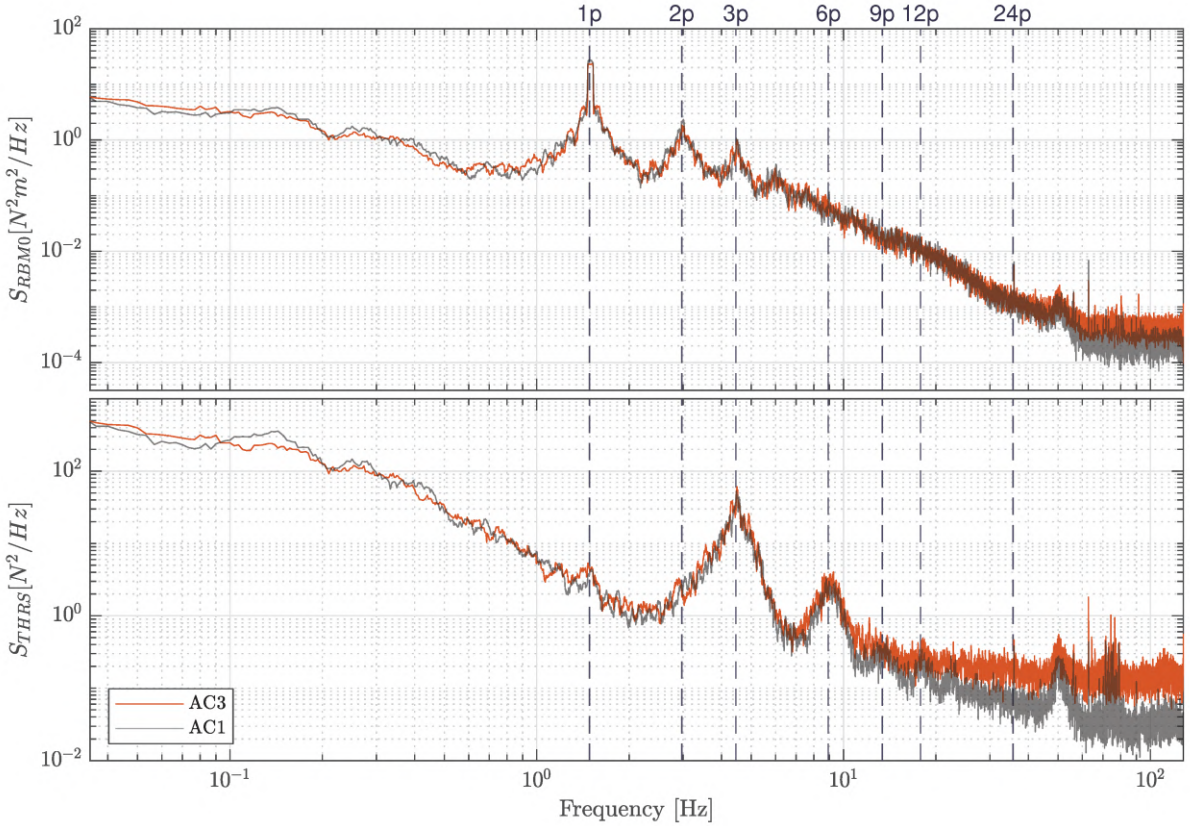

Figure 20 – Spectral density plots of THR and RBM for a turbine in an array (AC3) and solo (AC1) [10].

4. RESULTS

4.1 Correlation Observations

As a first control, Figure 21 and Figure 22 show power and thrust coefficients that have been plotted against TSR for the test tanks belonging to the FloWave batch where TSR ranges from 3 to 12. Error shows 5th to 95th percentiles of the measurements. The sampling frequency of these tests were all set to 256 Hz and ran for 300 seconds. The aspect of these curves, which is similar to conventional performance curves for horizontal axis turbines, attests for the validity of the next analyses done on the other non-dimensional variables.

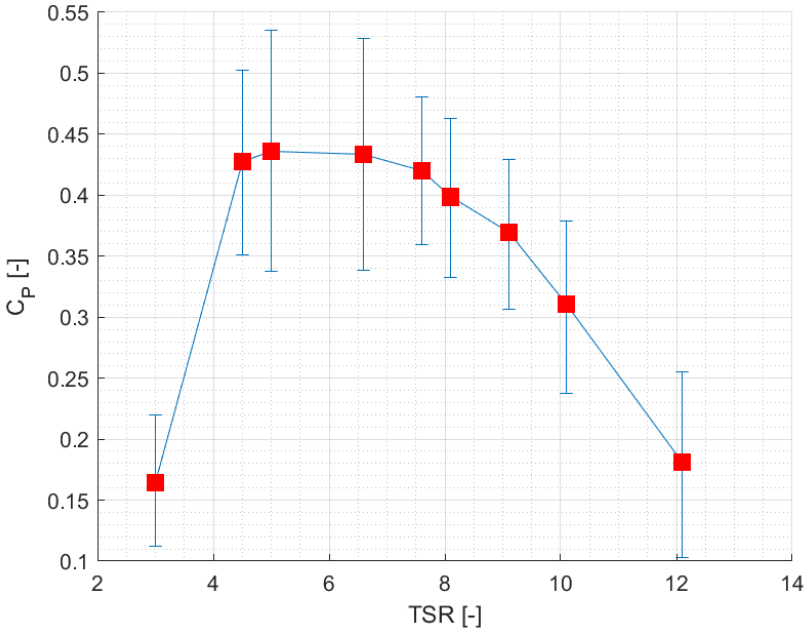

Figure 21 – C_P vs TSR for the FloWave tank tests.

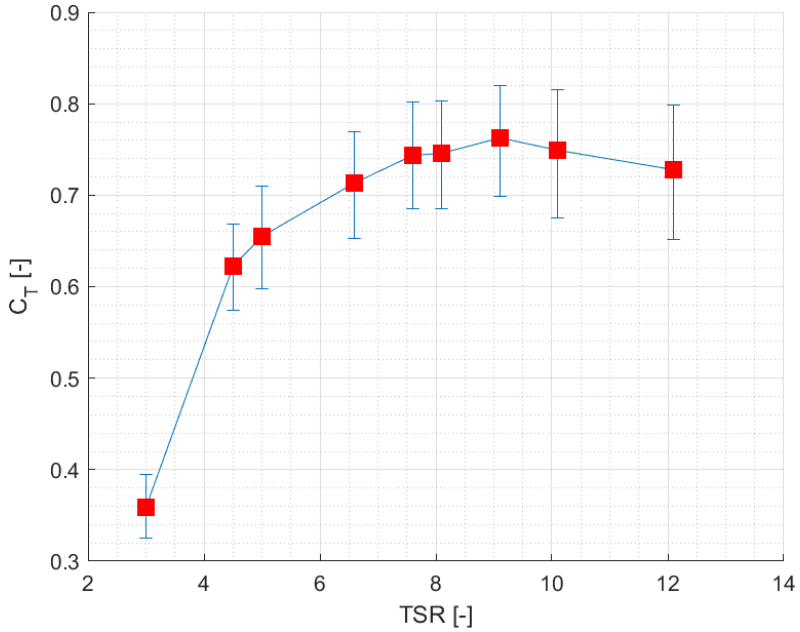

Figure 22 –C_T vs TSR for the FloWave tank tests.

Figure 23 includes all the datasets analysed in this task. The frequency in all datasets has been normalised to the rotational frequency. At three times the rotational frequency, or 3P, a spike can be observed where the power coefficient suffers a pulse, resulting in an increase of this value. For the Sabella D10 turbine, periodic pulsations at 1P and 5P are caused by the tower shadow effect every time a blade passes through the structure.

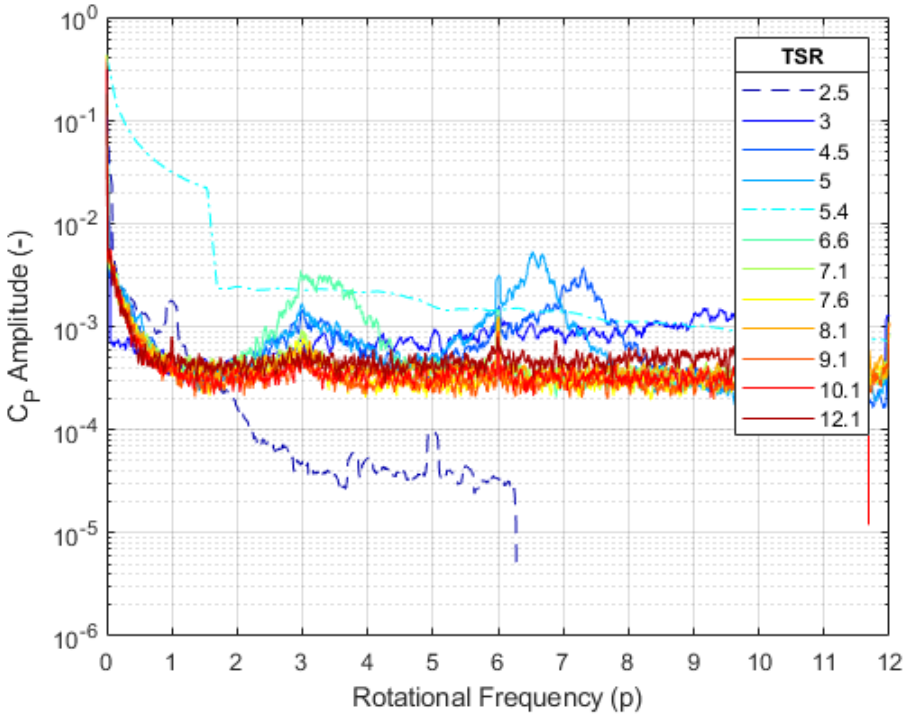

Figure 23 – Power coefficient spectra for base tests. (Dashed line belongs to D10, dash-dot line to CFD-BEMT)

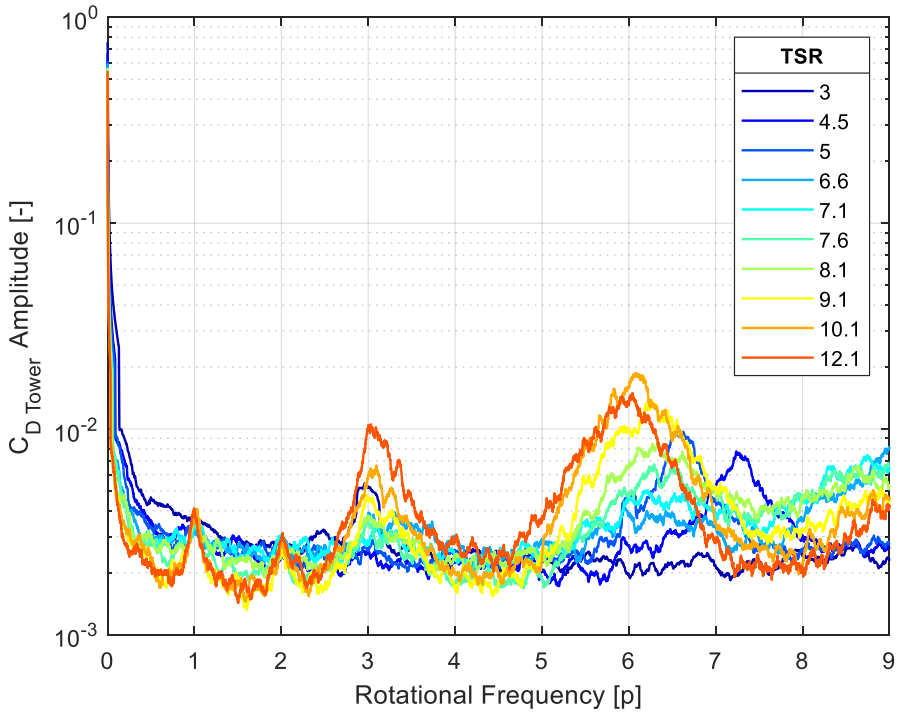

Figure 24 – Tower drag coefficient spectra for different FloWave tank tests.

Figure 24 shows the spectra of the drag coefficient experienced by the tower structure in the 10 base tests. This significant pulse has a recurrence of 3P, showing the highest peak at 6P. A correlation between the TSR and the amplitude of these pulses implies that higher TSRs convolutes the pulses towards this recurrence. This periodic fluctuation is an inherent characteristic of a three-bladed turbine, as its frequency can be calculated as the number of blades times the rotational frequency P [11]. The results from the Sabella datasets cannot be compared to this particular coefficient due to structure characteristics, where D10 has 4 towers holding the nacelle and D12 has no tower structure on the test rig.

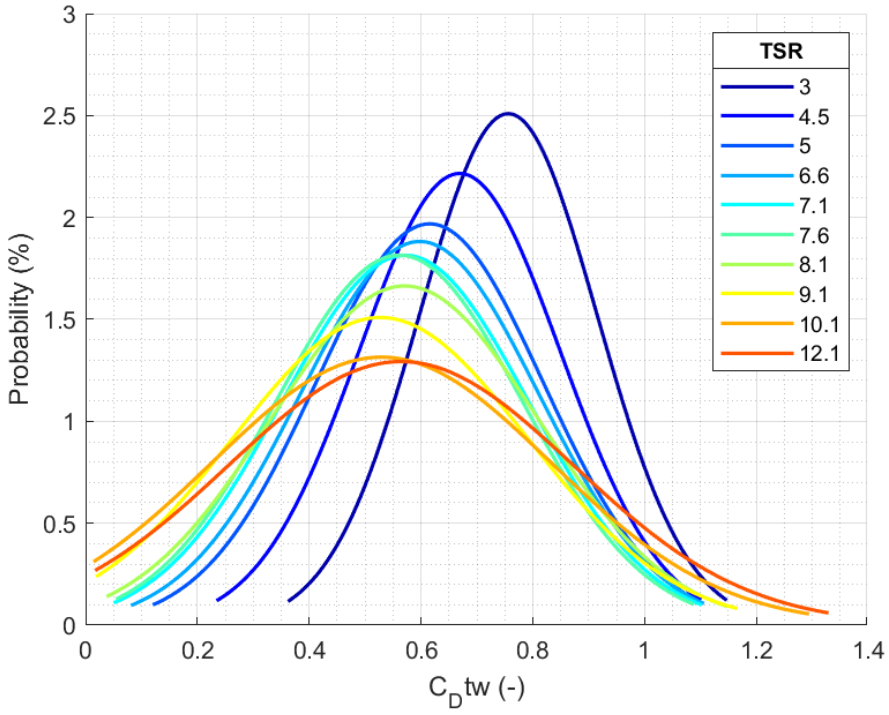

Figure 25 – Probability density distribution of the tower drag coefficient for different FloWave tank tests.

Analysing the distribution of the same variable, as seen in Figure 25, it is proven that a lower TSR results in a higher mean drag coefficient for the tower. This correlation is caused by the remaining kinetic energy that is not absorbed by a slow rotor, hitting the monopile. Although this structure might not be a vital concern for extreme load designs, fatigue failure due to these high vibratory loads can be expected to diminish the structure's service life.

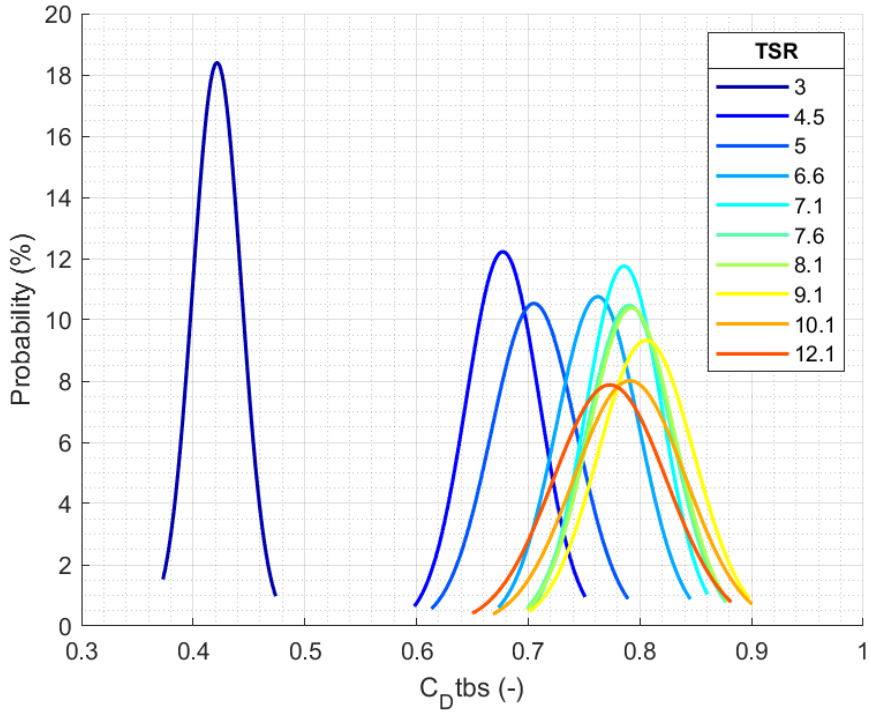

Figure 26 – Probability density distribution of the turbine drag coefficient for different FloWave tank tests.

Figure 26 shows the incidence of the surge reaction force at the foundation for the total drag coefficient of the turbine. Unlike the thrust coefficient calculated before, surge accounts for the drag generated by the whole structure, hence a lower TSR is proportionate to this calculated drag coefficient. The same can be said when analysing Figure 27, where the highest spike can be seen at 3P and returning with a decreased pulse at 6P.

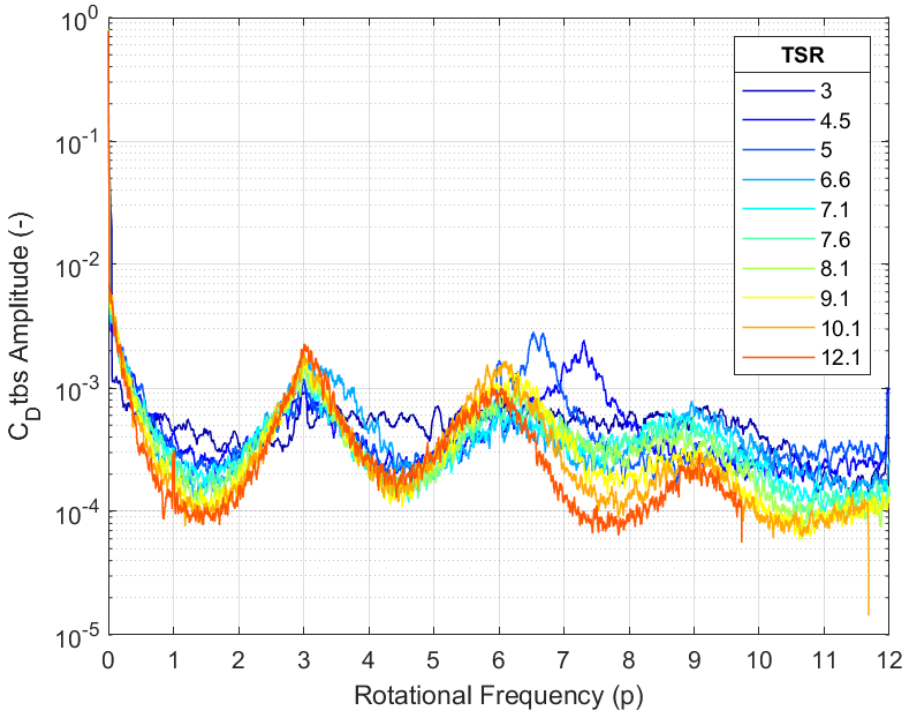

Figure 27 – Surge-based drag coefficient spectra for base tests.

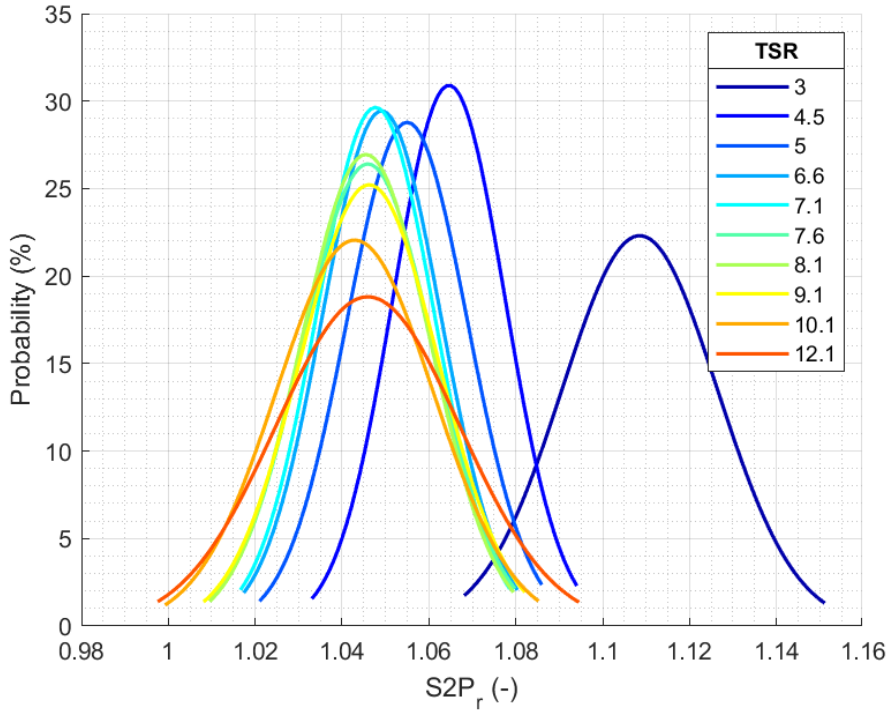

Figure 28 – Probability density distribution of surge to pitch ratio for different FloWave tank tests.

On the other hand, Figure 28 implies that a lower TSR incurs to a higher surge to pitch ratio. This assumption is only related to bottom-fixed turbines, as the pitch moment increases with the hub height. Figure 29 shows the frequency spectra for the same non-dimensional ratio and higher TSRs can be seen to follow the same pattern as previous coefficients where higher spikes are seen at 1P and every 3P, whereas lower TSRs shows a more evenly distributed amplitude across the rotational frequency axis.

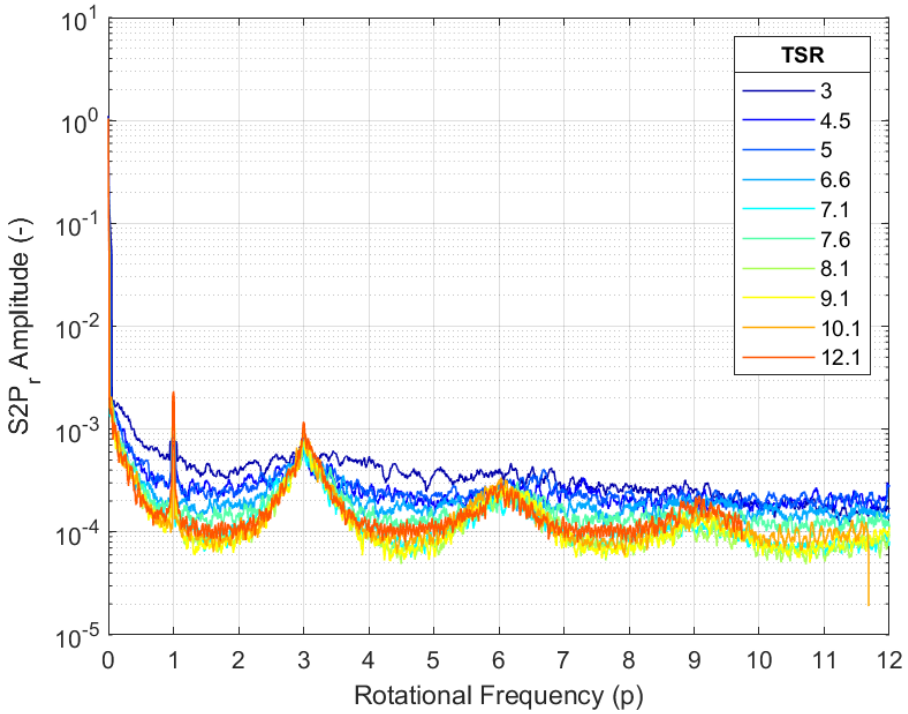

Figure 29 – Surge to pitch ratio spectra for base tests.

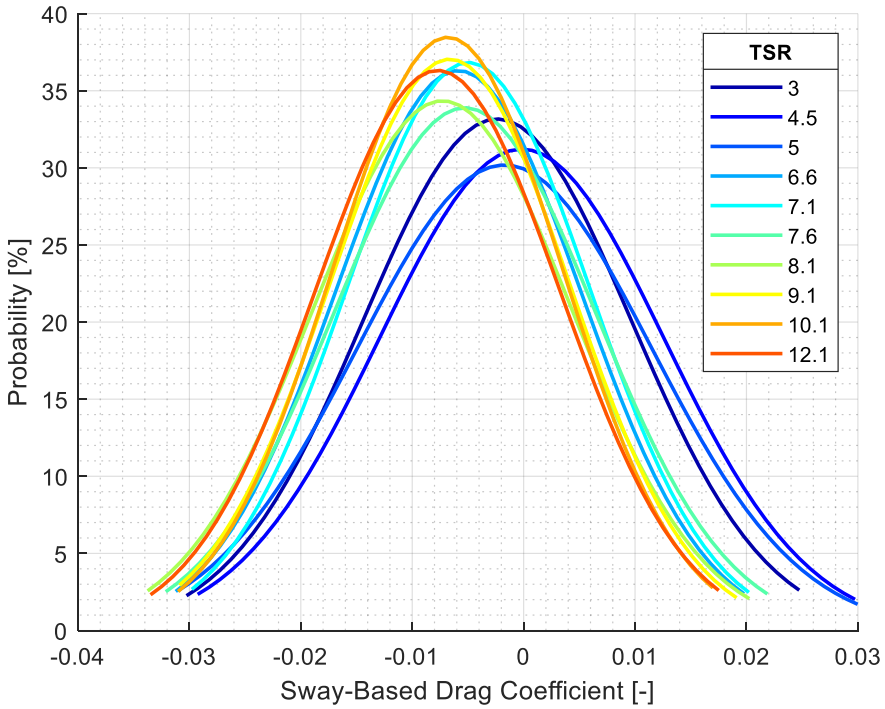

Figure 30 – Probability density distribution of turbine drag force on the y-direction for tank tests.

As none of the tests analysed are under yawed flow conditions, sway and therefore the drag coefficient in the y-direction should be negligible. Negative values in Figure 30 only accounts for sway forces in the other direction, which are caused by the direction of rotation of the rotor and the wake and vortex induced by this rotation. The biggest changes in this coefficient can only be seen in the frequency spectra in Figure 31, where the 3P effect is characteristic of a three-bladed turbine.

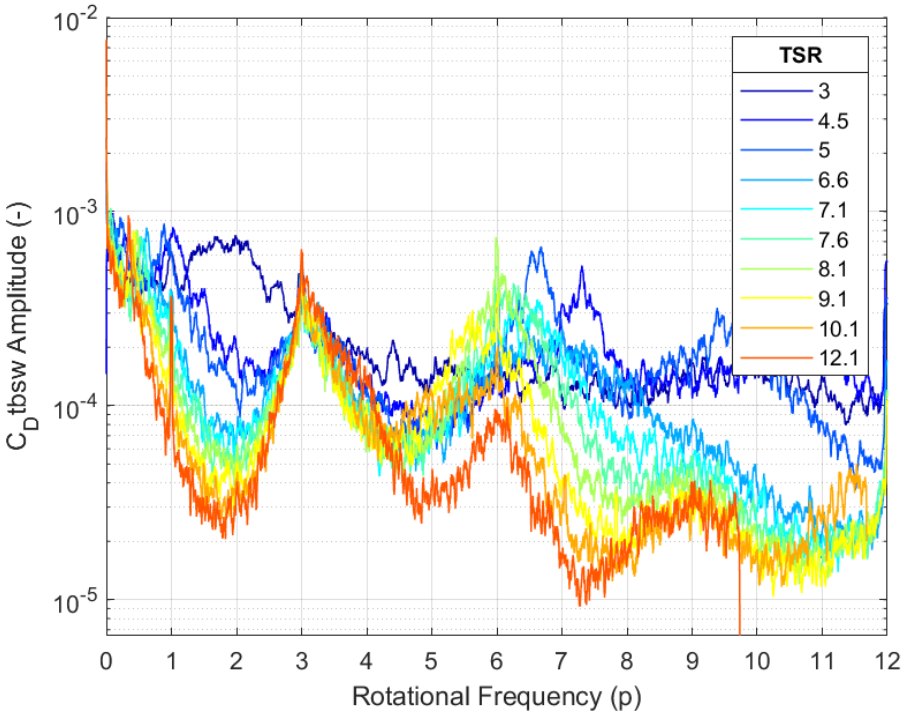

Figure 31 – Sway-based drag coefficient spectra for base tests.

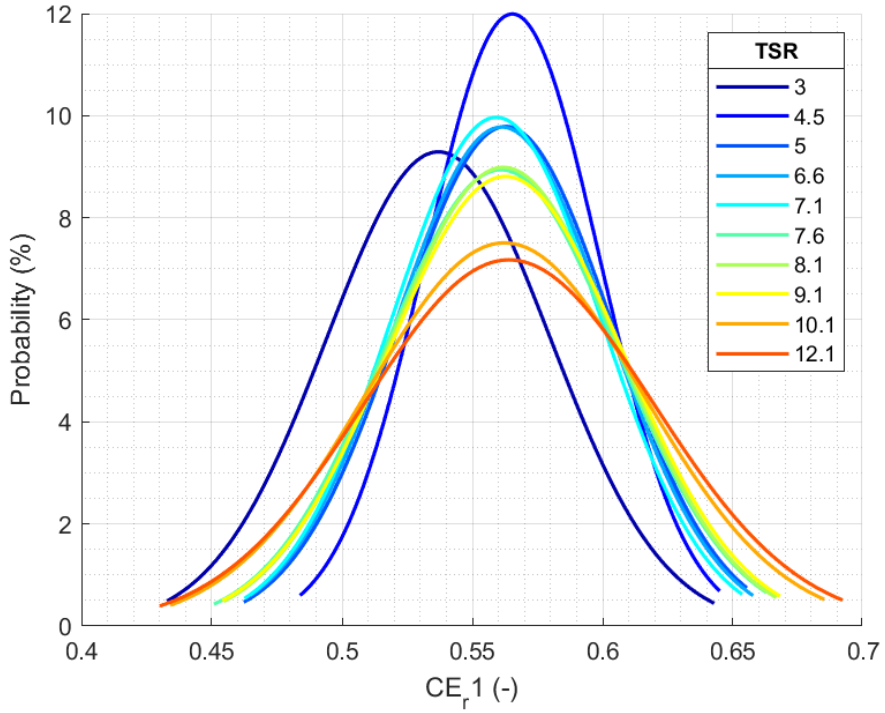

Figure 32 – Probability density distribution of centre of effort ratio on the blades for base tests.

Figure 32 shows the first non-dimensional variable calculated that compares the rotor thrust measurements with the root bending moment readings at the roots. As a result, a centre of effort shows dependency on the turbine parameters, where the curve for a TSR of 3 had a different setup compared to the rest of the tests on the batch. The frequency spectra, however, in Figure 33 shows a trend for every test where a decreasing spike generates a pulse every 1P, with an absence every 3P due to tower shadow effects.

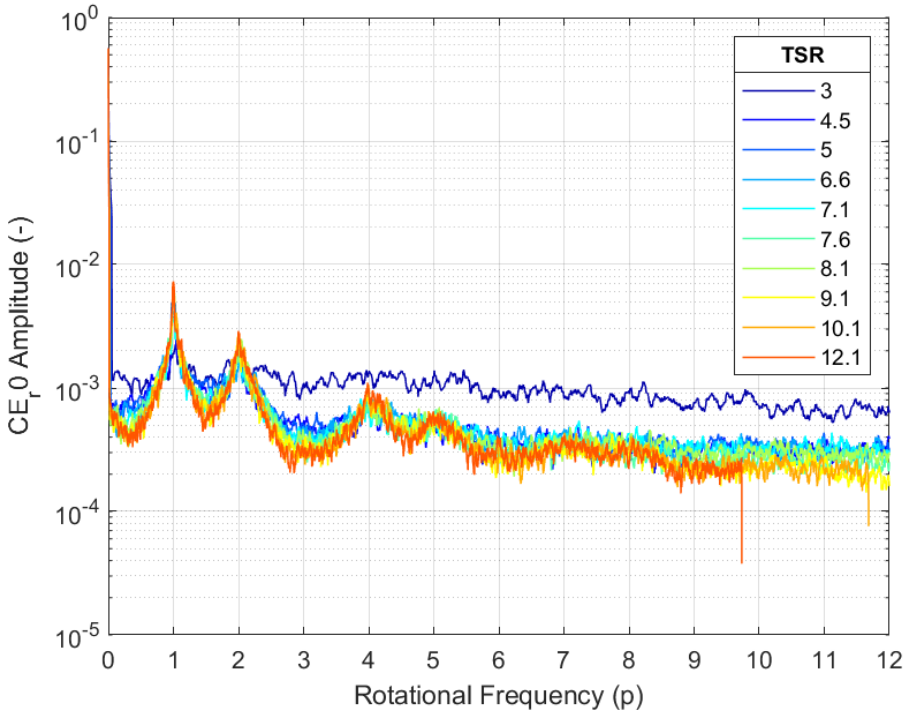

Figure 33 – Centre of effort ratio spectra for base tests.

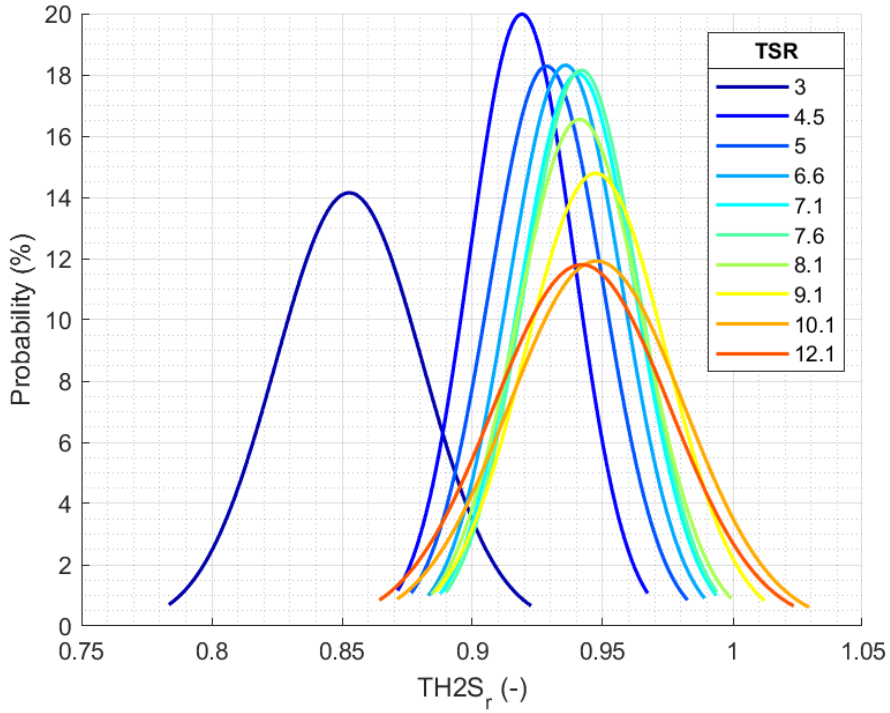

Figure 34 – Probability density distribution of thrust to surge ratio for different FloWave tank tests.

The thrust to surge ratio relates two input measurements from the datasets. Thrust is measured at the rotor and surge is captured by the loading cell underneath the tower. In the presence of any kind of support for the nacelle, these two values are not equal, as shown in Figure 34. Higher TSRs show a closer distribution to 1 as the fast-spinning blades divert the incoming flow from hitting the tower, thus reducing the drag coefficient of the monopile as well. The same interpretation can be drawn from Figure 35, where a high TSR reduces the amplitude on this ratio to frequencies below 6P.

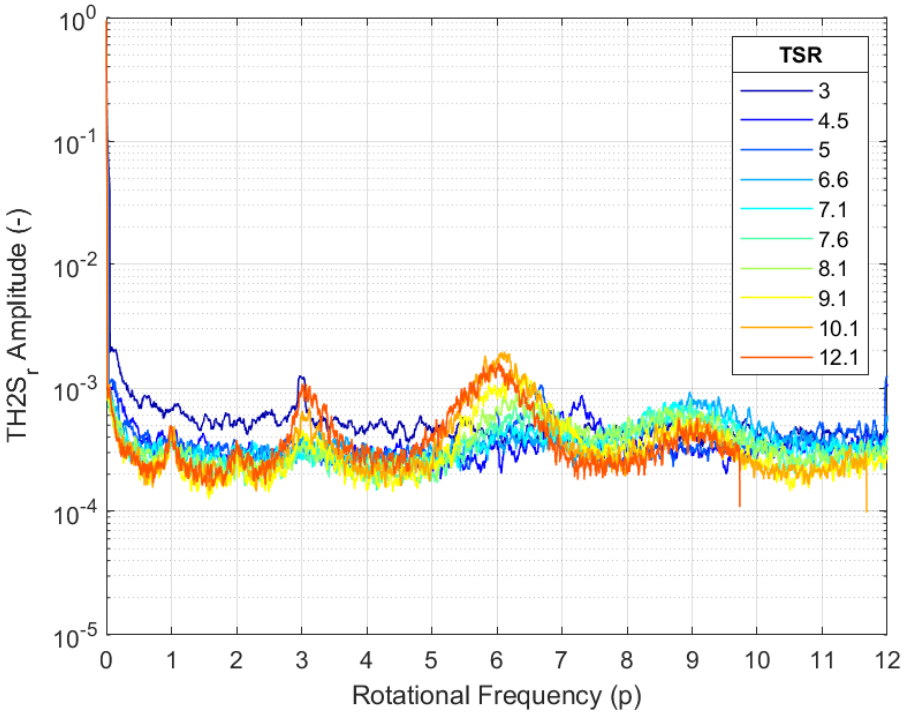

Figure 35 – Thrust to surge ratio spectra for base tests.

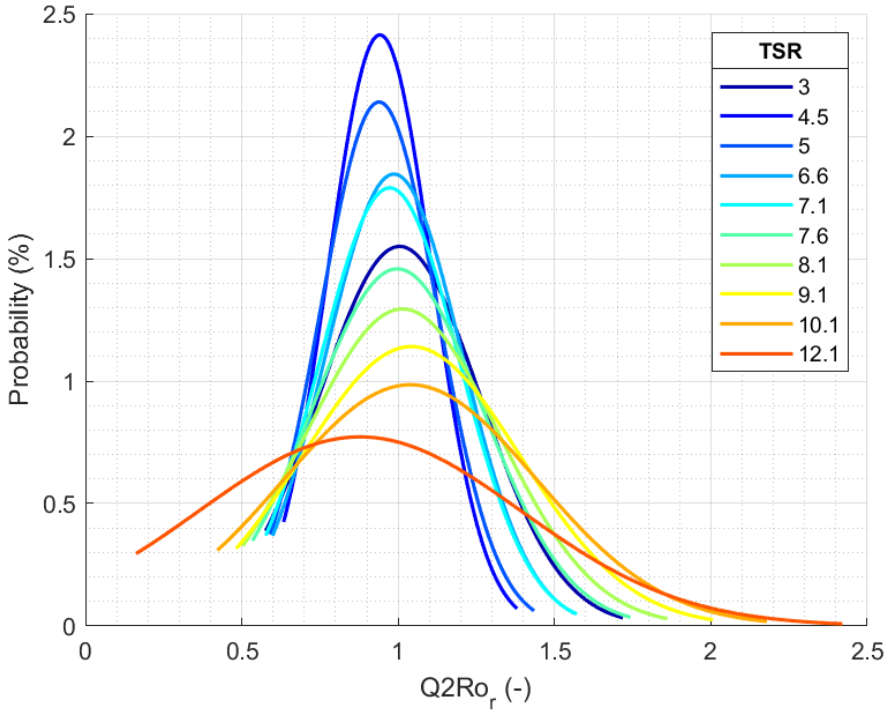

Figure 36 – Probability density distribution of the torque to roll ratio for different FloWave tank tests.

As the roll is measured at the foundation, the mechanical torque generated by the blades can generate substantial amounts of noise the higher the rotational speed, as shown in Figure 36. The standard deviation shows to be proportional to the TSR, meaning that high TSRs can generate undesired moments on the other axes. Furthermore, Figure 37 shows the ratio that relates the torque to the root bending moment measurements.

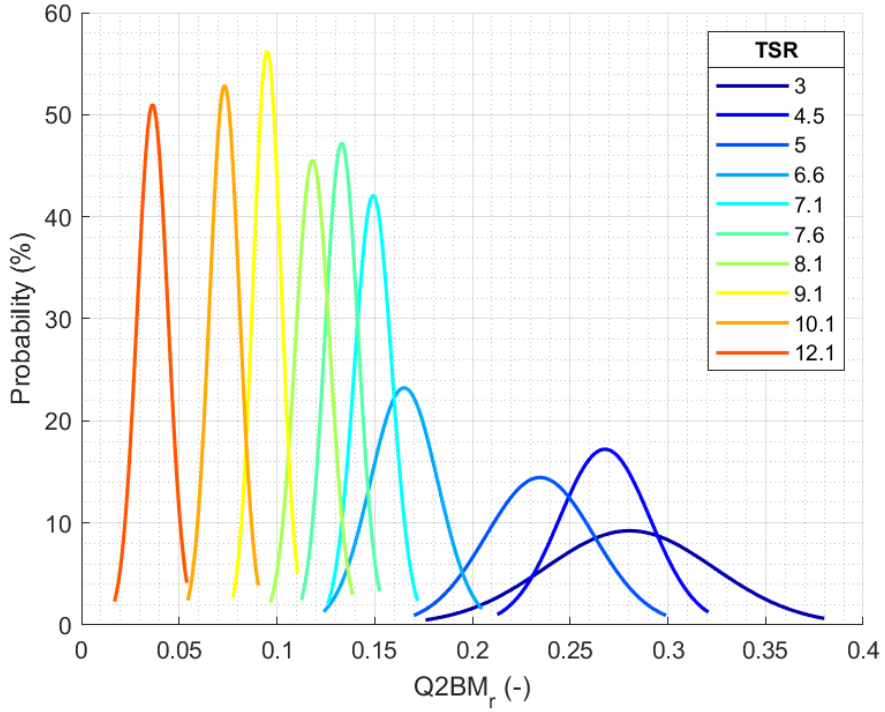

Figure 37 – Probability density distribution of the torque to RBM ratio for different FloWave tank tests.

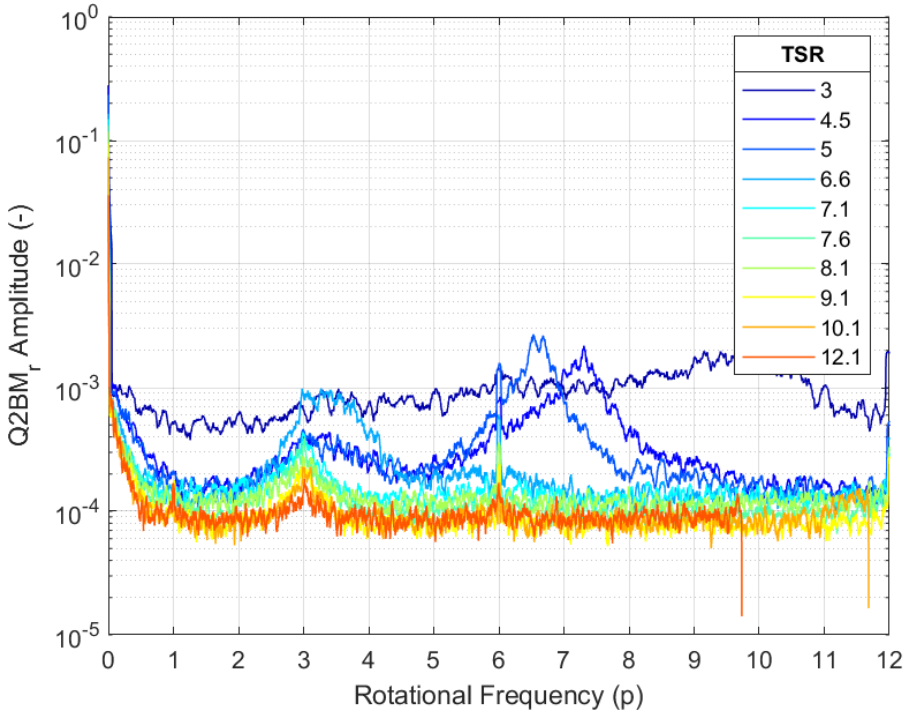

Figure 38 – Torque to RBMs ratio spectra for base tests.

As an addition to the information analysed from Figure 37, the frequency spectra of Figure 38 shows the impact of the 3P effect caused by the tower shadow on a ratio that only considers transducers located in front of the monopile structure. However, the impact is minimal compared to other ratios as the pulses do not show high spikes on the periodic 3P frequency. On the other hand, when analysing the ratio between two foundation measurements, sway and surge, a lower TSR creates undesired residual forces on the y-direction. These forces are linked to the rotational frequency, thus increasing the standard deviation of this non-dimensional ratio, as seen in Figure 39.

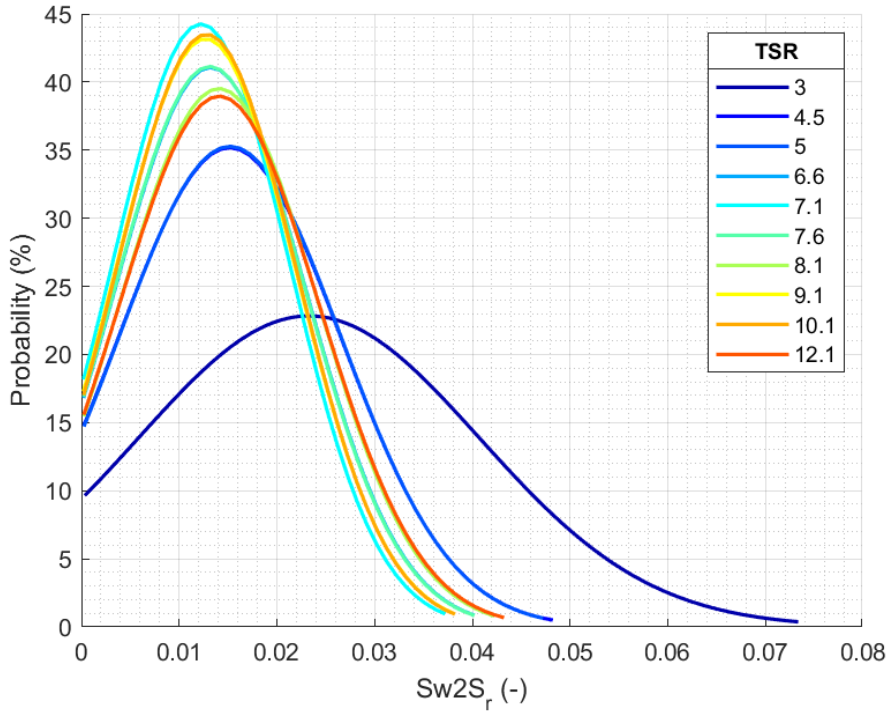

Figure 39 – Probability density distribution of sway to surge ratio for different FloWave tank tests.

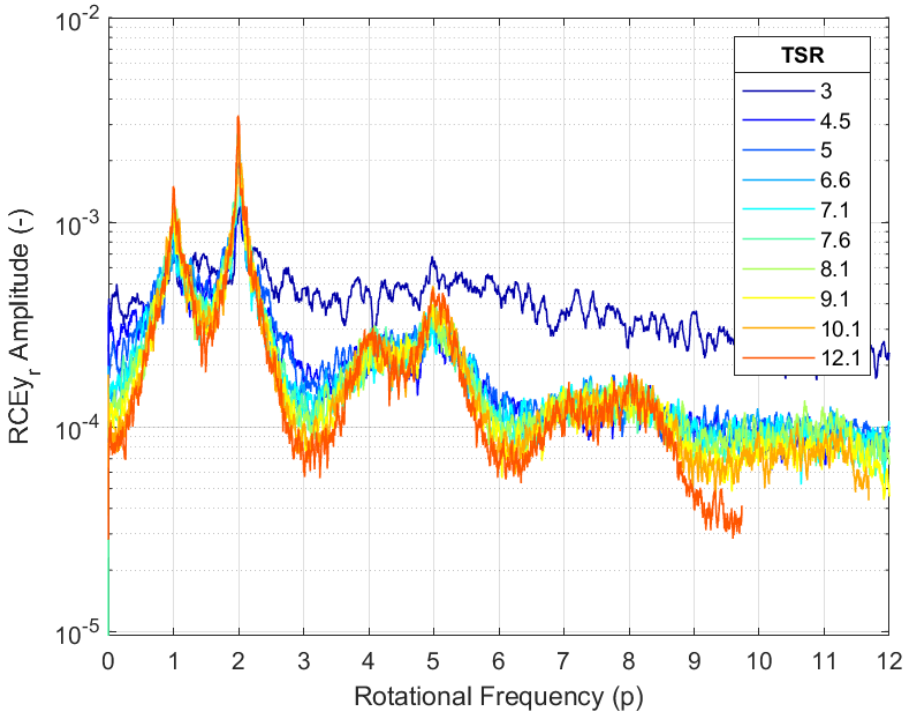

Figure 40 – Frequency spectra of the rotor's centre of effort on the y-direction.

Figure 40 describes the change on the centre of effort at the rotor in the y-direction. Under ideal conditions this would always be located at the axis of rotation, however, shear force, turbulence and the tower shadow effect create a recurring offset. The substantial spikes are pulsing at a 1P frequency as well as neglecting the 3P effect on this turbine.

Figure 41 shows a much more prevalent 3P effect, as the ratio analysed considers the change in the centre of effort of the tower in the z- direction. The difference in amplitudes across the rotation frequency is enhanced by the TSR value. The 1P pulsation is also visible in this ratio.

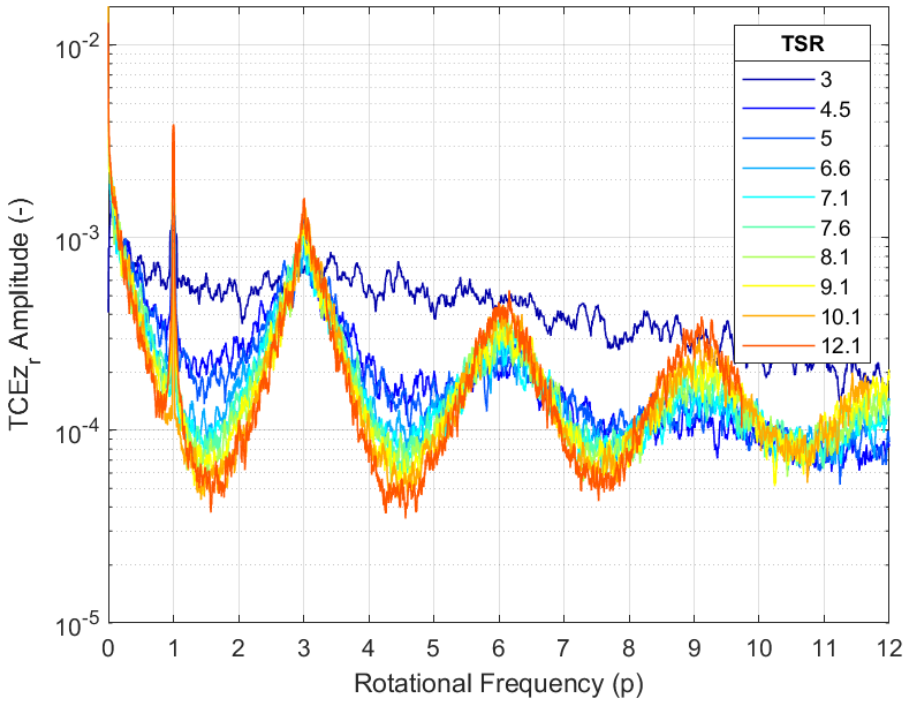

Figure 41 – Frequency spectra of the tower's centre of effort on the z-direction.

4.2 Data Base

As all the datasets created for this report are shared for further investigation to improve future designs, the dataset will be divided in 3 subsets:

- Metadata
- Non-dimensional time domain dataset (see Appendix 6.1)
- Non-dimensional frequency domain dataset (see Appendix 6.2)

These datasets are created in a NetCDF, which allows the data generated in this report to be self-describing and software independent [12]. A version has also been provided in comma separated value (CSV) file format to ease opening the data in software such as Microsoft Excel.

4.2.1 Metadata

The metadata includes information about the RealTide project, contact information, details of the test, and geometry properties specific to the turbine tested. An example table can be seen in Table 8, which is merged into the two other datasets.

Table 8 – Metadata example.

Properties	Description
Project	RealTide: Advanced monitoring, simulation, and control of tidal devices in unsteady, highly turbulent realistic tide environments
Work Package	WP3: Realistic Simulation of Tidal Turbine
Deliverable	D3.5: Synthetic Load Spectra and Time Series of Tidal Turbines
Organization	The University of Edinburgh
Author	Miguel Angel Valdivia Camacho
Supervisors	Dr Jeffrey Steynor, Prof David Ingram
Temporary Dataset URL	https://datasync.ed.ac.uk/index.php/s/CdTgK1bqHkyyGUF Password: R34lT!de
Contact	MA.Valdivia@ed.ac.uk, Jeff.Steynor@ed.ac.uk, David.Ingram@ed.ac.uk
Description	Internal Test ID: TC000#
Naming Convention	R = Reaction force, M = Reaction moment, 0,1,2 = blade number, r = rotor, s = shaft, n = nacelle, t = tower, o = origin, x, y, z = global direction
Units	f = Hz, RBM = N.m, TRQU = N.m, THRS = N, S = m^2.s, A = Variable, phi = rad
TSR	Variable tip speed ratio

4.2.2 Non-Dimensional Time Domain Data Subset

The non-dimensional time domain dataset, another main output of this deliverable, considers all the variables proposed for normalisation, as well as all the internal forces calculated related to the input data from the specific tests. Reaction forces and reaction moments are related to the rotor thrust and torque, respectively. The total time is variable across the different tests; however, they all consider measurements when the rotational speed reaches the value needed to achieve the TSR specified.

4.2.3 Non-Dimensional Frequency Domain Data Subset

The non-dimensional frequency domain dataset presents the frequency response of the system for all signals up to 25 Hz, equivalent of at least 12 times the rotational speed of the turbine. Every non-dimensional variable is stored in sinusoidal properties of energy density, amplitude, and phase angle for an easy access.

5. CONCLUSIONS

The Deliverable 3.5, synthetic load spectra and time series of tidal turbines, describes the activities carried out to develop the T3.5 under the RealTide project. Datasets from both experimental tests and numerical models have been gathered along with all the turbine characteristics and flow specifications. The experimental datasets available consist of 10 tank tests of a scaled generic hydrokinetic turbine in the FloWave facility. These tests shared the same geometry properties but differed in their tip speed ratios, ranging from 3 to 12. This first approach allowed tests from commercial turbines like the Sabella D10 and D12 to be compared using load measurements that are commonly retrieved regardless of the turbine structure.

Based on these measurements, a full calculation on the internal forces has been developed using free body diagrams on all the key components of the structure. A system of linear equations under static equilibrium made it possible to find reaction forces and moments in every joint and fixed end at any time step. A total of 21 non-dimensional coefficients and ratios have been proposed that effectively standardised all the tests studied in this report. Several of these non-dimensional coefficients captured the internal forces calculated in this task and related them to one of the different measurements in the input data to maintain a level of accuracy and reliability.

As the objectives of this deliverable are to present the analysis both as a time series and a frequency spectrum, the results have been described using probability density distributions and Fourier transforms. The power coefficient versus TSR and thrust coefficient versus TSR curves proved the base datasets to be acceptable to find normalised trends on the structure's behaviour when it is subjected to environmental conditions. For instance, the density distribution curves show the monopile drag coefficient to be inversely proportional to the TSR, however, the standard deviation increases and indicates a bigger impact on the fatigue life of the structure. This has been endorsed by looking at the frequency domain where a rotational frequency of 3P sees a surge in the coefficient's amplitude. A TSR of 12, the highest TSR tested in the FloWave facility among the datasets available, has also seen drastic shifts and spikes in 1P and 2P.

Another coefficient that shows the importance of the TSR on the load profile is the centre of effort at the blade. This ratio relates the thrust, the flapwise root bending moments, and the swept area. When analysing the density distribution curves of this ratio, all datasets available had similar values between 0.5 and 0.6, however, a trend could only be seen when analysing the frequency spectra. High TSR values showed a higher frequency clustering around every rotational pulse, which indicates that the resultant drag forces acting on the blades constantly change of position and pressure is not evenly distributed on blade elements from numerical models. In essence, analysing the spectra generated for all the non-dimensional coefficients proposed shows a characterised increase of the different load amplitudes and vibration prevalence with higher TSRs, which can be detrimental for the turbine's service life.

Most of the spikes or pulses seen in the frequency spectra curves can be traced back to the tower shadow effect and the 3P effect, that has an impact on the loading cases as well as the total power generation. As the base datasets of this study consist of a three-bladed turbine attached to a monopile structure, different setups might differ when comparing non-dimensional coefficients related to foundation loads. In that sense, more tests with different support designs would refine these coefficients and ratios to compare the impact of the categorised tower designs on the loading profiles and energy extraction.

The newly developed normalised datasets have been uploaded to the Edinburgh DataShare portal, an open sharing digital repository for future tidal turbines design to consider as checkpoints throughout their development. These datasets are stored in an open-source format and can be easily recreated to visualise the structure's behaviour. Each of the dataset files contain metadata information about the test, and most importantly the TSR. Every test has been further divided in two files to comply with the objective of this deliverable to have both a time series and a frequency domain series. This approach allows designs to be considered both under static and fatigue load profiles.

6. APPENDICES

6.1 List of Time Domain Variables

Name	Description	Units
Time	Step	s
RPM	Rotational speed	rpm
ANG0	Blade 0 angular position	º
ANG1	Blade 1 angular position	º
ANG2	Blade 2 angular position	º
RBM0	Root bending moment	N.m
RBM1	Root bending moment	N.m
RBM2	Root bending moment	N.m
TRQ	Rotor torque	N.m
THR	Rotor thrust	N
P	Instantaneous power	W
CE_0	Centre of Effort Blade 0	m
CE_1	Centre of Effort Blade 1	m
CE_2	Centre of Effort Blade 2	m
CE_r0	CoE ratio Blade 0	-
CE_r1	CoE ratio Blade 1	-
CE_r2	CoE ratio Blade 2	-
TSR	Tip speed ratio	-
C_P	Power coefficient	-
C_T	Thrust coefficient	-
C_TRBM	RBM-based thrust coefficient	-
C_Dtbs	Surge-based drag coefficient	-
C_Dtbp	Pitch-based drag coefficient	-
C_Dtbsw	Sway-based drag coefficient	-
C_Dtw	Tower drag coefficient	-
Sw2S_r	Sway to surge ratio	-
Hv2S_r	Heave to surge ratio	-
TH2S_r	Thrust to surge ratio	-
S2P_r	Surge to pitch ratio	-
Q2Ro_r	Torque to roll ratio	-
Q2BM_r	Torque to RBMs ratio	-
RPitch_r	Rotor pitch ratio	-
RRoll_r	Rotor roll ratio	-
RYaw_r	Rotor yaw ratio	-
RCEy_r	Rotor's CoE in y ratio	-
RCEz_r	Rotor's CoE in z ratio	-
TCEy_r	Tower's CoE in y ratio	-
TCEz_r	Tower's CoE in z ratio	-
R0x	Blade0 reaction force in x	N
R0y	Blade0 reaction force in y	N
R0z	Blade0 reaction force in z	N
M0x	Blade0 reaction moment in x	N.m
M0y	Blade0 reaction moment in y	N.m

Name	Description	Units
M0z	Blade0 reaction moment in z	N.m
R1x	Blade1 reaction force in x	N
R1y	Blade1 reaction force in y	N
R1z	Blade1 reaction force in z	N
M1x	Blade1 reaction moment in x	N.m
M1y	Blade1 reaction moment in y	N.m
M1z	Blade1 reaction moment in z	N.m
R2x	Blade2 reaction force in x	N
R2y	Blade2 reaction force in y	N
R2z	Blade2 reaction force in z	N
M2x	Blade2 reaction moment in x	N.m
M2y	Blade2 reaction moment in y	N.m
M2z	Blade2 reaction moment in z	N.m
Rrx	Rotor reaction force in x	N
Rry	Rotor reaction force in y	N
Rrz	Rotor reaction force in z	N
Mrx	Rotor reaction moment in x	N.m
Mry	Rotor reaction moment in y	N.m
Mrz	Rotor reaction moment in z	N.m
Rsx	Shaft reaction force in x	N
Rsy	Shaft reaction force in y	N
Rsz	Shaft reaction force in z	N
Msx	Shaft reaction moment in x	N.m
Msy	Shaft reaction moment in y	N.m
Msz	Shaft reaction moment in z	N.m
Rnx	Nacelle reaction force in x	N
Rny	Nacelle reaction force in y	N
Rnz	Nacelle reaction force in z	N
Mnx	Nacelle reaction moment in x	N.m
Mny	Nacelle reaction moment in y	N.m
Mnz	Nacelle reaction moment in z	N.m
Rtx	Tower reaction force in x	N
Rty	Tower reaction force in y	N
Rtz	Tower reaction force in z	N
Mtx	Tower reaction moment in x	N.m
Mty	Tower reaction moment in y	N.m
Mtz	Tower reaction moment in z	N.m
Rox	Origin reaction force in x	N
Roy	Origin reaction force in y	N
Roz	Origin reaction force in z	N
Mox	Origin reaction moment in x	N.m
Moy	Origin reaction moment in y	N.m
Moz	Origin reaction moment in z	N.m

6.2 List of Frequency Domain Variables

Name	Descriptor	Units
f	Frequency	Hz
RPM_S	Energy	m^2.s
RPM_A	Amplitude	rpm
RPM_phi	Phase	rad/s
ANG0_S	Energy	m^2.s
ANG0_A	Amplitude	º
ANG0_phi	Phase	rad/s
ANG1_S	Energy	m^2.s
ANG1_A	Amplitude	º
ANG1_phi	Phase	rad/s
ANG2_S	Energy	m^2.s
ANG2_A	Amplitude	º
ANG2_phi	Phase	rad/s
RBM0_S	Energy	m^2.s
RBM0_A	Amplitude	N.m
RBM0_phi	Phase	rad/s
RBM1_S	Energy	m^2.s
RBM1_A	Amplitude	N.m
RBM1_phi	Phase	rad/s
RBM2_S	Energy	N.m
RBM2_A	Amplitude	N.m
RBM2_phi	Phase	rad/s
TRQ_S	Energy	N.m
TRQ_A	Amplitude	N.m
TRQ_phi	Phase	rad/s
THR_S	Energy	N
THR_A	Amplitude	N.m
THR_phi	Phase	rad/s
P_S	Energy	W
P_A	Amplitude	N.m
P_phi	Phase	rad/s
CE_0_S	Energy	m
CE_0_A	Amplitude	N.m
CE_0_phi	Phase	rad/s
CE_1_S	Energy	m
CE_1_A	Amplitude	N.m
CE_1_phi	Phase	rad/s
CE_2_S	Energy	m
CE_2_A	Amplitude	N.m
CE_2_phi	Phase	rad/s
CE_r0_S	Energy	m^2.s

Name	Descriptor	Units
CE_r0_A	Amplitude	-
CE_r0_phi	Phase	rad/s
CE_r1_S	Energy	m^2.s
CE_r1_A	Amplitude	-
CE_r1_phi	Phase	rad/s
CE_r2_S	Energy	m^2.s
CE_r2_A	Amplitude	-
CE_r2_phi	Phase	rad/s
TSR_S	Energy	m^2.s
TSR_A	Amplitude	-
TSR_phi	Phase	rad/s
C_P_S	Energy	m^2.s
C_P_A	Amplitude	-
C_P_phi	Phase	rad/s
C_T_S	Energy	m^2.s
C_T_A	Amplitude	-
C_T_phi	Phase	rad/s
C_TRBM_S	Energy	m^2.s
C_TRBM_A	Amplitude	-
C_TRBM_phi	Phase	rad/s
C_Dtbs_S	Energy	m^2.s
C_Dtbs_A	Amplitude	-
C_Dtbs_phi	Phase	rad/s
C_Dtbp_S	Energy	m^2.s
C_Dtbp_A	Amplitude	-
C_Dtbp_phi	Phase	rad/s
C_Dtbsw_S	Energy	m^2.s
C_Dtbsw_A	Amplitude	-
C_Dtbsw_phi	Phase	rad/s
C_Dtw_S	Energy	m^2.s
C_Dtw_A	Amplitude	-
C_Dtw_phi	Phase	rad/s
Sw2S_r_S	Energy	m^2.s
Sw2S_r_A	Amplitude	-
Sw2S_r_phi	Phase	rad/s
Hv2S_r_S	Energy	m^2.s
Hv2S_r_A	Amplitude	-
Hv2S_r_phi	Phase	rad/s
TH2S_r_S	Energy	m^2.s
TH2S_r_A	Amplitude	-
TH2S_r_phi	Phase	rad/s

Name	Descriptor	Units
S2P_r_S	Energy	m^2.s
S2P_r_A	Amplitude	-
S2P_r_phi	Phase	rad/s
Q2Ro_r_S	Energy	m^2.s
Q2Ro_r_A	Amplitude	-
Q2Ro_r_phi	Phase	rad/s
Q2BM_r_S	Energy	m^2.s
Q2BM_r_A	Amplitude	-
Q2BM_r_phi	Phase	rad/s
RPitch_r_S	Energy	m^2.s
RPitch_r_A	Amplitude	-
RPitch_r_phi	Phase	rad/s
RRoll_r_S	Energy	m^2.s
RRoll_r_A	Amplitude	-
RRoll_r_phi	Phase	rad/s
RYaw_r_S	Energy	m^2.s
RYaw_r_A	Amplitude	-
RYaw_r_phi	Phase	rad/s
RCEy_r_S	Energy	m^2.s
RCEy_r_A	Amplitude	-
RCEy_r_phi	Phase	rad/s
RCEz_r_S	Energy	m^2.s
RCEz_r_A	Amplitude	-
RCEz_r_phi	Phase	rad/s
TCEy_r_S	Energy	m^2.s
TCEy_r_A	Amplitude	-
TCEy_r_phi	Phase	rad/s
TCEz_r_S	Energy	m^2.s
TCEz_r_A	Amplitude	-
TCEz_r_phi	Phase	rad/s
R0x_S	Energy	m^2.s
R0x_A	Amplitude	N
R0x_phi	Phase	rad/s
R0y_S	Energy	m^2.s
R0y_A	Amplitude	N
R0y_phi	Phase	rad/s
R0z_S	Energy	m^2.s
R0z_A	Amplitude	N
R0z_phi	Phase	rad/s
M0x_S	Energy	m^2.s
M0x_A	Amplitude	N.m

Name	Descriptor	Units
M0x_phi	Phase	rad/s
M0y_S	Energy	m^2.s
M0y_A	Amplitude	N.m
M0y_phi	Phase	rad/s
M0z_S	Energy	m^2.s
M0z_A	Amplitude	N.m
M0z_phi	Phase	rad/s
R1x_S	Energy	m^2.s
R1x_A	Amplitude	N
R1x_phi	Phase	rad/s
R1y_S	Energy	m^2.s
R1y_A	Amplitude	N
R1y_phi	Phase	rad/s
R1z_S	Energy	m^2.s
R1z_A	Amplitude	N
R1z_phi	Phase	rad/s
M1x_S	Energy	m^2.s
M1x_A	Amplitude	N.m
M1x_phi	Phase	rad/s
M1y_S	Energy	m^2.s
M1y_A	Amplitude	N.m
M1y_phi	Phase	rad/s
M1z_S	Energy	m^2.s
M1z_A	Amplitude	N.m
M1z_phi	Phase	rad/s
R2x_S	Energy	m^2.s
R2x_A	Amplitude	N
R2x_phi	Phase	rad/s
R2y_S	Energy	m^2.s
R2y_A	Amplitude	N
R2y_phi	Phase	rad/s
R2z_S	Energy	m^2.s
R2z_A	Amplitude	N
R2z_phi	Phase	rad/s
M2x_S	Energy	m^2.s
M2x_A	Amplitude	N.m
M2x_phi	Phase	rad/s
M2y_S	Energy	m^2.s
M2y_A	Amplitude	N.m
M2y_phi	Phase	rad/s
M2z_S	Energy	m^2.s

Name	Descriptor	Units
M2z_A	Amplitude	N.m
M2z_phi	Phase	rad/s
Rrx_S	Energy	m^2.s
Rrx_A	Amplitude	N
Rrx_phi	Phase	rad/s
Rry_S	Energy	m^2.s
Rry_A	Amplitude	N
Rry_phi	Phase	rad/s
Rrz_S	Energy	m^2.s
Rrz_A	Amplitude	N
Rrz_phi	Phase	rad/s
Mrx_S	Energy	m^2.s
Mrx_A	Amplitude	N.m
Mrx_phi	Phase	rad/s
Mry_S	Energy	m^2.s
Mry_A	Amplitude	N.m
Mry_phi	Phase	rad/s
Mrz_S	Energy	m^2.s
Mrz_A	Amplitude	N.m
Mrz_phi	Phase	rad/s
Rsx_S	Energy	m^2.s
Rsx_A	Amplitude	N
Rsx_phi	Phase	rad/s
Rsy_S	Energy	m^2.s
Rsy_A	Amplitude	N
Rsy_phi	Phase	rad/s
Rsz_S	Energy	m^2.s
Rsz_A	Amplitude	N
Rsz_phi	Phase	rad/s
Msx_S	Energy	m^2.s
Msx_A	Amplitude	N.m
Msx_phi	Phase	rad/s
Msy_S	Energy	m^2.s
Msy_A	Amplitude	N.m
Msy_phi	Phase	rad/s
Msz_S	Energy	m^2.s
Msz_A	Amplitude	N.m
Msz_phi	Phase	rad/s
Rnx_S	Energy	m^2.s
Rnx_A	Amplitude	N
Rnx_phi	Phase	rad/s

Name	Descriptor	Units
Rny_S	Energy	m^2.s
Rny_A	Amplitude	N
Rny_phi	Phase	rad/s
Rnz_S	Energy	m^2.s
Rnz_A	Amplitude	N
Rnz_phi	Phase	rad/s
Mnx_S	Energy	m^2.s
Mnx_A	Amplitude	N.m
Mnx_phi	Phase	rad/s
Mny_S	Energy	m^2.s
Mny_A	Amplitude	N.m
Mny_phi	Phase	rad/s
Mnz_S	Energy	m^2.s
Mnz_A	Amplitude	N.m
Mnz_phi	Phase	rad/s
Rtx_S	Energy	m^2.s
Rtx_A	Amplitude	N
Rtx_phi	Phase	rad/s
Rty_S	Energy	m^2.s
Rty_A	Amplitude	N
Rty_phi	Phase	rad/s
Rtz_S	Energy	m^2.s
Rtz_A	Amplitude	N
Rtz_phi	Phase	rad/s
Mtx_S	Energy	m^2.s
Mtx_A	Amplitude	N.m
Mtx_phi	Phase	rad/s
Mty_S	Energy	m^2.s
Mty_A	Amplitude	N.m
Mty_phi	Phase	rad/s
Mtz_S	Energy	m^2.s
Mtz_A	Amplitude	N.m
Mtz_phi	Phase	rad/s
Rox_S	Energy	m^2.s
Rox_A	Amplitude	N
Rox_phi	Phase	rad/s
Roy_S	Energy	m^2.s
Roy_A	Amplitude	N
Roy_phi	Phase	rad/s
Roz_S	Energy	m^2.s
Roz_A	Amplitude	N

Name	Descriptor	Units
Roz_phi	Phase	rad/s
Mox_S	Energy	m^2.s
Mox_A	Amplitude	N.m
Mox_phi	Phase	rad/s
Moy_S	Energy	m^2.s
Moy_A	Amplitude	N.m
Moy_phi	Phase	rad/s
Moz_S	Energy	m^2.s
Moz_A	Amplitude	N.m
Moz_phi	Phase	rad/s